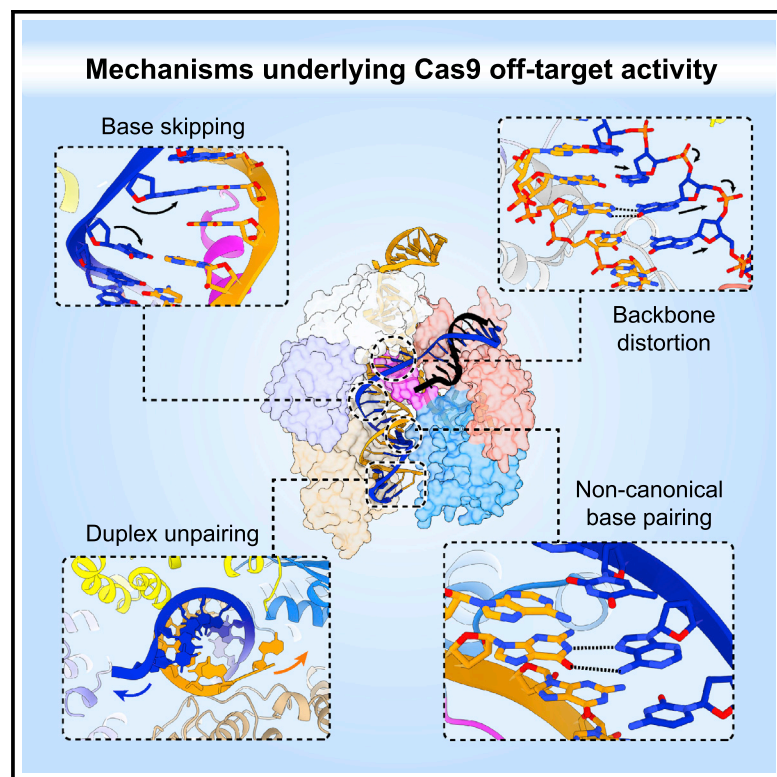


Structural basis for Cas9 off-target activity

Graphical abstract



Authors

Martin Pacesa, Chun-Han Lin, Antoine Cléry, ..., Peter Cameron, Paul D. Donohoue, Martin Jinek

Correspondence

jinek@bioc.uzh.ch

In brief

19 structures of Cas9 bound to on- and off-target DNAs provide insights into many ways through which Cas9 can recognize off-target sites, with implications for the development of high-fidelity Cas9 variants, guide RNA design, and off-target prediction.

Highlights

- 19 crystal structures of Cas9 bound to on- and off-target DNA substrates
- Mismatch tolerance is enabled by formation of non-canonical base pairs
- Single-nucleotide deletions are accommodated by base skipping or multiple mismatches
- PAM-distal mismatches perturb the REC2/REC3 conformational checkpoint



Article

Structural basis for Cas9 off-target activity

Martin Pacesa,¹ Chun-Han Lin,^{2,5} Antoine Cléry,³ Aakash Saha,⁴ Pablo R. Arantes,⁴ Katja Bargsten,^{1,6} Matthew J. Irby,^{2,7} Frédéric H.-T. Allain,³ Giulia Palermo,⁴ Peter Cameron,^{2,8} Paul D. Donohoue,² and Martin Jinek^{1,9,*}

¹Department of Biochemistry, University of Zurich, Winterthurerstrasse 190, 8057 Zurich, Switzerland

²Caribou Biosciences, 2929 Seventh Street Suite 105, Berkeley, CA 94710, USA

³Institute of Biochemistry, ETH Zurich, Höggerbergring 64, 8093 Zurich, Switzerland

⁴Department of Bioengineering, University of California Riverside, 900 University Avenue, Riverside, CA 92512, USA

⁵Present address: LinkedIn, Sunnyvale, CA 94085, USA

⁶Present address: leadXpro AG, Villigen, Switzerland

⁷Present address: Prime Medicine, Cambridge, MA 02139, USA

⁸Present address: Spotlight Therapeutics, Hayward, CA 94545, USA

⁹Lead contact

*Correspondence: jinek@bioc.uzh.ch

<https://doi.org/10.1016/j.cell.2022.09.026>

SUMMARY

The target DNA specificity of the CRISPR-associated genome editor nuclease Cas9 is determined by complementarity to a 20-nucleotide segment in its guide RNA. However, Cas9 can bind and cleave partially complementary off-target sequences, which raises safety concerns for its use in clinical applications. Here, we report crystallographic structures of Cas9 bound to bona fide off-target substrates, revealing that off-target binding is enabled by a range of noncanonical base-pairing interactions within the guide:off-target heteroduplex. Off-target substrates containing single-nucleotide deletions relative to the guide RNA are accommodated by base skipping or multiple noncanonical base pairs rather than RNA bulge formation. Finally, PAM-distal mismatches result in duplex unpairing and induce a conformational change in the Cas9 REC lobe that perturbs its conformational activation. Together, these insights provide a structural rationale for the off-target activity of Cas9 and contribute to the improved rational design of guide RNAs and off-target prediction algorithms.

INTRODUCTION

Cas9, the effector nuclease of prokaryotic type II CRISPR adaptive immune systems (Makarova et al., 2020), cleaves double-stranded DNA (dsDNA) substrates complementary to a guide CRISPR RNA (crRNA) (Jinek et al., 2012). By changing the sequence of the guide RNA (gRNA), the target DNA specificity of the CRISPR-Cas9 system is readily programmable (Jinek et al., 2012), a feature that has been widely exploited for genome engineering applications (Anzalone et al., 2020). Cas9 functions in conjunction with a *trans*-activating crRNA (tracrRNA), which is required both for crRNA loading and subsequent DNA binding and cleavage (Deltcheva et al., 2011; Jinek et al., 2012). Target DNA binding and cleavage are further dependent on the presence of a protospacer-adjacent motif (PAM) flanking the target sequence (Anders et al., 2014; Jinek et al., 2012). Due to its high activity and 5'-NGG-3' PAM specificity, *Streptococcus pyogenes* Cas9 (SpCas9) remains the most widely used CRISPR-Cas nuclease for gene editing applications. However, despite a high intrinsic accuracy in generating targeted DNA breaks, SpCas9 can nevertheless cleave genomic DNA sequences with imperfect complementarity to the gRNA, resulting in off-target editing (Cameron et al., 2017; Hsu et al., 2013; Pattanayak

et al., 2013; Tsai et al., 2015). The off-target activity of SpCas9, as well as other Cas9 enzymes, thus presents a safety concern for their therapeutic applications.

Off-target sites typically contain one or several nucleobase mismatches relative to the gRNA (Cameron et al., 2017; Tsai et al., 2015, 2017). Recent studies have established that the type of mismatch, its positioning, and the total number of mismatches are important determinants of off-target DNA binding and cleavage (Boyle et al., 2017, 2021; Doench et al., 2016; Jones et al., 2021; Zhang et al., 2020). PAM-proximal mismatches within the seed region of the gRNA-target strand (TS) DNA heteroduplex typically have a dramatic impact on substrate DNA binding and R-loop formation (Boyle et al., 2021; Ivanov et al., 2020; Singh et al., 2016; Zhang et al., 2020). In contrast, PAM-distal mismatches are compatible with stable binding; however, their presence often results in the formation of a catalytically incompetent complex (Boyle et al., 2021; Dagdas et al., 2017; Ivanov et al., 2020; Jones et al., 2021; Sternberg et al., 2015; Yang et al., 2018; Zhang et al., 2020). Moreover, Cas9 has been shown to cleave off-target substrates containing insertions or deletions relative to the gRNA sequence, which have been proposed to be recognized through the formation of nucleotide “bulges” in the gRNA-TS DNA heteroduplex (Boyle et al.,



2021; Cameron et al., 2017; Doench et al., 2016; Jones et al., 2021; Lin et al., 2014; Tsai et al., 2015).

Numerous computational tools have been developed to predict possible genomic off-target sites based on sequence similarity (Bae et al., 2014; Stemmer et al., 2015). However, the majority of actual off-target cleavage events remain unpredicted (Cameron et al., 2017; Tsai et al., 2015). Furthermore, although Cas9 is able to bind genomic sites harboring as few as five complementary nucleotides, only a relatively small number of off-target sites are actually cleaved and result in detectable off-target editing in cells (Kuscu et al., 2014; O'Geen et al., 2015; Wu et al., 2014). Several structures of target-bound Cas9 complexes have been determined to date (Anders et al., 2014; Jiang et al., 2016; Nishimasu et al., 2014; Zhu et al., 2019) that have shed light on the mechanism of on-target binding and cleavage. However, the same processes for off-target sites remain poorly understood.

To elucidate the mechanism of mismatch tolerance of Cas9, we determined crystal structures of a comprehensive set of bona fide off-target-bound complexes. These structures reveal that the formation of noncanonical base pairs and preservation of heteroduplex shape underpin the off-target tolerance of Cas9. We also observe that multiple consecutive mismatches can be accommodated by base skipping of a gRNA nucleotide, as opposed to nucleotide bulging. Finally, the structure of an off-target complex containing three PAM-distal mismatches exhibits REC2/3 domain rearrangements, which likely perturbs conformational activation of Cas9 and thus modulates cleavage efficiency. Taken together, our structural data reveal the diversity of mechanisms enabling off-target recognition and lay the foundation for improved off-target prediction and engineering optimized CRISPR-Cas9 complex designs for gene editing.

RESULTS

In vitro profiling reveals diversity of Cas9 off-targets

Multiple studies have investigated the off-target activity of Cas9, suggesting context-dependent tolerance of nucleobase mismatches between the gRNA and off-target DNA sequences (Boyle et al., 2021; Cameron et al., 2017; Lazzarotto et al., 2020; Tsai et al., 2015; Zhang et al., 2020). To investigate the effect of mismatches on Cas9 binding and cleavage, we performed the SITE-Seq assay (Cameron et al., 2017) to define the off-target landscapes of 12 well-studied gRNAs to select suitable off-targets for further evaluation (Figures S1A and S1B; Table S1). The SITE-Seq assay analysis revealed a total of 3,848 detectable off-target sites at the highest Cas9 ribonucleoprotein (RNP) concentration, with a median of 5 mismatches per off-target site (Figure S1C). The detected mismatches covered all possible base mismatch combinations and were distributed throughout the length of the gRNA-TS DNA heteroduplex (Figures S1D, S1E, S1G, and S1H).

To probe the thermodynamics of on- and off-target substrate DNA binding and the kinetics of DNA cleavage, we focused on a subset of four gRNAs (AAVS1, FANCF, PTPRC-tgt2, and TRAC) and a total of 15 bona fide off-target sites detectable *in vivo* (Cameron et al., 2017; Donohoue et al., 2021; Tsai et al., 2017, 2015)

(Figure 1A) that covered all 12 possible base mispair types. *In vitro* nuclease activity assays revealed that all selected off-target sequences were cleaved slower than the corresponding on-target substrates, with 20- to 500-fold reductions in the observed rate constants (Table 1; Figure S2A). To distinguish whether the cleavage defects were due to slow R-loop formation or perturbations in downstream steps, we also quantified cleavage kinetics using partially single-stranded PAM-presenting (PAMmer) DNA substrates (Anders et al., 2014; O'Connell et al., 2014). These experiments revealed that the slower cleavage kinetics of most off-target substrates was due to perturbed R-loop formation (Table 1; Figure S2B). However, for some off-targets, notably AAVS1 off-targets #2 and #5, FANCF off-targets #3, #4, and #6, and PTPRC-tgt2 off-target #1, the rate of PAMmer substrate cleavage was more than 100-fold slower compared with their respective on-target sequences (Table 1; Figure S2B), indicating perturbations in the conformational activation checkpoint downstream of guide-target hybridization or inhibition of cleavage by direct steric hindrance of the Cas9 HNH domain (Chen et al., 2017; Dagdas et al., 2017).

Complementary quantification of substrate DNA binding using DNA nanolever (switchSENSE) methodology revealed perturbations in the binding affinities of most off-targets (Table 1; Data S1). Notably, the reductions in binding affinities were almost entirely due to increased dissociation rates (k_{off}), while on-binding rates (k_{on}) were largely unperturbed (Table 1), indicating that most of the tested off-targets promote DNA dissociation, likely due to R-loop collapse. However, there was little correlation between the observed reductions in cleavage rates and binding constants (Figure S2C), confirming that the molecular basis for off-target discrimination by Cas9 is not based on substrate binding alone, in agreement with prior studies (Boyle et al., 2021; Chen et al., 2017; Dagdas et al., 2017; Jones et al., 2021; Yang et al., 2018; Zhang et al., 2020). The dissociation rate (k_{off}) correlated significantly only with the number of mismatches located in the seed region ($R^2 = 0.46$, $p = 0.001$) (Figure S2C), suggesting that seed mismatches promote R-loop collapse and non-target strand (NTS) rehybridization (Boyle et al., 2017; Gong et al., 2018; Singh et al., 2016; Sternberg et al., 2014).

Furthermore, we compared the measured cleavage rate constants (k_{obs}) with predicted data from a leading biophysical model of Cas9 off-target cleavage that accounts for mismatch number and position but utilizes position-independent weights for mismatch type (Jones et al., 2021). Despite good overall correlation between the model and our data ($R^2 = 0.46$, $p = 0.004$) (Figure S2C), there were several prominent outliers (AAVS1 off-target #2 and off-target #3 and FANCF off-target #4), suggesting that accurate modeling of off-target interactions requires accounting for position-specific effects of individual mismatch types (Figure S2D).

Finally, to benchmark the editing efficiency of the selected off-target substrates *in vivo*, we transfected human primary T cells with recombinant Cas9 RNPs at multiple concentrations and quantified indel frequencies. We observed efficient cellular editing at the on-target site for each gRNA at all RNP concentrations and detected editing at 7 of the 15 off-target sites in our set, including the deletion-containing FANCF off-target #3 (Figures S2E and S2F; Table S2), which contained a

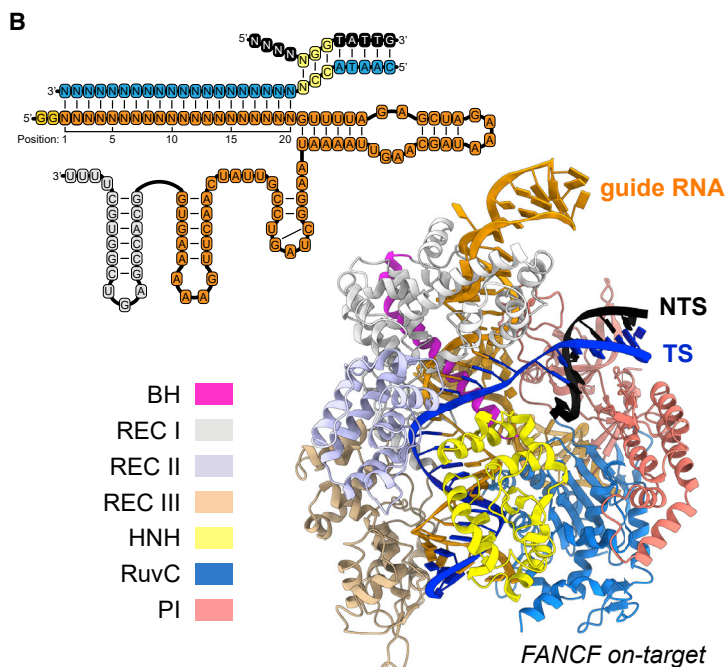
A

Gene	sequence	0	1	2	3	4	5	6	7	8	9	10	11	12	13	14	15	16	17	18	19	20	P	A	M
AAVS1	guide RNA	G	G	G	G	G	C	C	A	C	U	A	G	G	G	A	C	A	G	G	A	U			
AAVS1	on-target	C	C	C	C	G	G	T	G	A	T	C	C	C	T	G	T	C	C	T	A	A	C	C	
AAVS1	off-target1	.	.	.	T	.	.	.	A	G	C	C	C	
AAVS1	off-target2	A	.	.	.	C	.	G	T	G	A	A	C	C	
AAVS1	off-target3	C	C	T	C	C	
AAVS1	off-target4	A	A	T	A	C	C	
AAVS1	off-target5	.	.	.	T	C	G	G	A	C	C

FANCF	guide RNA	G	G	G	A	A	U	C	C	C	U	U	C	U	G	C	A	G	C	A	C	C		
FANCF	on-target	C	C	T	T	A	G	G	G	A	A	G	A	C	G	T	C	G	T	G	G	A	C	C
FANCF	off-target1	G	.	.	.	C	T	C	C
FANCF	off-target2	.	.	.	C	G	.	.	T	T	C	C
FANCF	off-target3	G	.	.	C	G	G	C	C
FANCF	off-target4	T	G	G	G	A	C	C
FANCF	off-target5	A	T	.	.	G	A	C	C
FANCF	off-target6	.	.	.	G	T	A	T	C	C
FANCF	off-target7	T	.	.	.	A	.	T	T	C	C

PTPRC-tgt2	guide RNA	G	G	C	A	A	A	C	U	C	A	A	C	C	C	U	A	C	C	C	C		
PTPRC-tgt2	on-target	C	G	T	T	T	G	A	G	T	T	G	G	G	A	T	G	G	G	G	A	C	C
PTPRC-tgt2	off-target1	T	.	.	.	A	.	.	T	A	C	C

TRAC	guide RNA	G	A	G	A	G	U	C	U	C	U	C	A	G	C	U	G	G	U	A	C	A		
TRAC	on-target	T	C	T	C	A	G	A	G	A	G	T	C	G	A	C	C	A	T	G	T	G	C	C
TRAC	off-target1	C	T	G	.	.	.	G	A	T	A	C	C	
TRAC	off-target2	.	T	T	T	A	C	C	



mismatch-reverting single-nucleotide polymorphism (SNP) relative to the reference human genome sequence.

Crystallographic analysis of off-target interactions

To obtain insights into the structural basis of off-target recognition and mismatch tolerance, we employed a previously described approach (Anders et al., 2014) to co-crystallize Cas9 with single-guide RNAs (sgRNAs) and partially duplexed off-target DNA substrates (Figure 1C). Focusing on our set of

Figure 1. Biochemical and structural analysis of Cas9 off-targets

(A) Guide RNA and (off)-target DNA sequences selected for biochemical and structural analysis. Matching bases in off-targets are denoted by a dot; nucleotide mismatches and deletions (-) are highlighted.

(B) Top: schematic representation of the guide RNA (orange), target DNA strand (blue), and non-target DNA strand (black) sequences used for crystallization. The PAM sequence in the DNA is highlighted in yellow. Bottom: structure of the Cas9 FANCF on-target complex. Individual Cas9 domains are colored according to the legend; substrate DNA target strand (TS) is colored blue, non-target strand (NTS) black, and the guide RNA orange.

See also Figures S1–S3.

AAVS1, FANCF, PTPRC-tgt2, and TRAC off-targets (Figure 1A), covering all 12 possible mismatch types, we determined a total of 15 off-target complex structures at resolutions of 2.25–3.30 Å (Figure 1C; Table S3). Overall, the off-target complex structures have very similar conformations, with the Cas9 polypeptide backbone superimposing with a mean root-mean-square deviation of 0.41 Å over 1,330 Cα atoms (as referenced to the FANCF on-target complex structure, excluding FANCF off-target #4, as discussed below). Of note, the AAVS1 on-target complex structure reveals substantial repositioning of the REC2 domain, which undergoes a 12° rotation (relative to FANCF and TRAC on-target complexes) (Figure S3A; Video S1), with concomitant shortening of the α-helix comprising residues 301–305 and restructuring of the loop comprising residues 175–179, enabled by the absence of crystal contacts involving the REC2 and REC3 domains.

However, the structures display considerable local variation of the gRNA-TS DNA heteroduplex conformation (Table S4). Base pairing and base stacking are mostly preserved throughout the heteroduplexes (Table S4), with the exception of positions

1–3 within the PAM-distal end of the guide-TS duplex, where the presence of mismatches results in duplex unpairing (Figures S3B–S3E). Interestingly, such unpairing results in the base stacking of the 5'-terminal residue of the sgRNA on top of the unpaired DNA base, as observed in a recent cryo-EM structure of a PAM-distal mismatch off-target complex (Bravo et al., 2022). Despite the observed conformational variation, the off-target structures preserve almost all intermolecular contacts between the Cas9 protein and the bound nucleic acids (Figure S3F), further

Table 1. Kinetic and thermodynamic analysis of off-target substrate binding and cleavage

Gene	Target	24-h cleavage (%)	k_{obs} (min^{-1})	k_{on} ($\text{M}^{-1} \cdot \text{s}^{-1}$)	k_{off} (s^{-1})	K_{d} (μM)	24-h cleavage (%) PAMmer	k_{obs} (min^{-1}) PAMmer
AAVS1	on-target	92.2	1.624 ± 0.159	$3.95 \pm 0.26 \times 10^6$	$5.74 \pm 0.73 \times 10^{-5}$	14.5 ± 2.1	95.0	0.562 ± 0.073
AAVS1	off-target #1	92.7	0.071 ± 0.005	$4.73 \pm 0.71 \times 10^6$	$6.29 \pm 0.29 \times 10^5$	13.3 ± 2.1	87.5	0.239 ± 0.031
AAVS1	off-target #2	95.1	0.034 ± 0.002	$8.75 \pm 0.31 \times 10^6$	$3.38 \pm 0.08 \times 10^{-3}$	386 ± 16	85.5	0.004 ± 0.0001
AAVS1	off-target #3	96.7	0.051 ± 0.002	$3.30 \pm 0.11 \times 10^6$	$2.51 \pm 0.15 \times 10^{-3}$	761 ± 51	82.7	0.081 ± 0.010
AAVS1	off-target #4	94.4	0.004 ± 0.0002	$1.09 \pm 0.03 \times 10^7$	$3.28 \pm 0.06 \times 10^{-3}$	301 ± 9	89.6	0.065 ± 0.007
AAVS1	off-target #5	18.9	0.00013 ± 0.0003	ND	ND	ND	70.1	0.007 ± 0.0001
FANCF	on-target	97.5	0.238 ± 0.013	$3.45 \pm 0.19 \times 10^6$	$7.46 \pm 0.97 \times 10^{-5}$	21.6 ± 3.1	98.3	0.565 ± 0.054
FANCF	off-target #1	35.1	0.001 ± 0.0001	$3.97 \pm 0.06 \times 10^6$	$2.09 \pm 0.06 \times 10^{-3}$	528 ± 17	97.4	0.069 ± 0.006
FANCF	off-target #2	62.4	0.001 ± 0.0002	$1.42 \pm 0.03 \times 10^6$	$2.45 \pm 0.06 \times 10^{-3}$	$1,730 \pm 60$	92.9	0.233 ± 0.018
FANCF	off-target #3	0.0	0	$1.22 \pm 0.05 \times 10^7$	$2.37 \pm 0.11 \times 10^{-3}$	193 ± 13	4.2	0.00003 ± 0.0003
FANCF	off-target #4	53.0	0.0005 ± 0.0002	$3.35 \pm 0.05 \times 10^6$	$1.91 \pm 0.07 \times 10^{-3}$	571 ± 24	38.9	0.001 ± 0.0001
FANCF	off-target #5	80.4	0.001 ± 0.0001	$1.27 \pm 0.05 \times 10^6$	$2.55 \pm 0.10 \times 10^{-3}$	$2,010 \pm 110$	92.9	0.058 ± 0.005
FANCF	off-target #6	8.2	0.00006 ± 0.0003	$1.50 \pm 0.09 \times 10^6$	$2.03 \pm 0.15 \times 10^{-3}$	$1,350 \pm 130$	66.6	0.001 ± 0.00005
FANCF	off-target #7	5.2	0.004 ± 0.0003	$2.95 \pm 0.20 \times 10^6$	$3.21 \pm 0.23 \times 10^{-3}$	$1,090 \pm 110$	94.5	0.013 ± 0.001
PTPRC-tgt2	on-target	96.8	0.459 ± 0.022	$6.08 \pm 0.39 \times 10^6$	$2.19 \pm 0.21 \times 10^{-4}$	36.0 ± 4.2	95.5	0.074 ± 0.015
PTPRC-tgt2	off-target #1	0.0	0	$1.22 \pm 0.07 \times 10^7$	$2.39 \pm 0.12 \times 10^{-3}$	196 ± 15	91.4	0.001 ± 0.0003
TRAC	on-target	97.7	0.381 ± 0.015	$1.02 \pm 0.21 \times 10^6$	$3.23 \pm 0.53 \times 10^{-4}$	31.8 ± 8.5	93.5	0.181 ± 0.013
TRAC	off-target #1	95.8	0.019 ± 0.001	$1.37 \pm 0.45 \times 10^6$	$1.77 \pm 0.1 \times 10^{-4}$	130 ± 44	90.7	0.081 ± 0.006
TRAC	off-target #2	65.0	0.001 ± 0.00006	$9.43 \pm 1.12 \times 10^6$	$3.27 \pm 0.27 \times 10^{-4}$	34.6 ± 5.0	88.4	0.026 ± 0.002

Kinetic and thermodynamic parameters of off-target substrates. The cleavage rate constants (k_{obs}) were derived from single-exponential function fitting of measured cleavage rates of the target-strand labeled DNA substrates. The binding and dissociation rate constants (k_{on} and k_{off}) and the equilibrium dissociation constant (K_{d}) were determined using a DNA nanolever binding (switchSENSE) assay. Intervals indicate standard error of mean. See also [Figure S2](#).

underscoring the structural plasticity of Cas9 in accommodating mismatch-induced heteroduplex distortions.

Noncanonical base-pairing interactions facilitate off-target recognition

A substantial fraction of the base mismatches observed in the determined off-target complex structures (34 of 49) is accommodated by noncanonical base-pairing interactions that preserve at least one hydrogen bond between the mispaired bases. The most common off-target mismatches, both in our dataset ([Table S1](#)) and as reported by other studies ([Boyle et al., 2017](#); [Doench et al., 2016](#); [Hsu et al., 2013](#); [Jones et al., 2021](#); [Pattanayak et al., 2013](#); [Zhang et al., 2020](#)), are rG-dT ([Figures S4A–S4G](#)) and rU-dG ([Figures 2A and S4H–S4N](#)), which have the potential to form wobble base pairs ([Kimsey et al., 2015](#)). Indeed, all rG-dT mismatches in the determined structures are accommodated by wobble base pairing. Observed at duplex positions 4, 13, and 15, the dT base undergoes an ~ 1 Å shear displacement into the major groove of the gRNA-TS DNA heteroduplex to form the wobble base pair ([Figures S4A–S4E](#)), whereas at duplex position 2, wobble base pairing is enabled by a minor-groove displacement of the rG base ([Figures S4F–S4G](#)). In contrast, rU-dG base pairs in the determined structures exhibit consider-

able structural variation. At duplex position 10, the rU base is able to undergo the major groove displacement required for wobble base pairing ([Figure 2A and S4H](#)). In contrast, at duplex position 5, the backbone of the RNA strand makes extensive contacts with Cas9 ([Figures S3 and S4I–S4K](#)), and as a result, the rU-dG base pairs are instead accommodated by compensatory shifts of the dG base to maintain hydrogen-bonding interactions ([Figures S4I–S4K](#)). At duplex position 9 in the TRAC off-target #1 complex, the rU-dG mismatch is accommodated by wobble base pairing enabled by a minor-groove displacement of the dG base ([Figure S4L](#)). At the same duplex position in the AAVS1 off-target #1 and #2 complexes, however, this mismatch occurs next to rC-dA and rC-dT mismatches, respectively, and adopts the sterically prohibited Watson-Crick geometry ([Figures S4M and S4N](#)), implying a tautomeric shift or base deprotonation to accommodate this otherwise unfavorable base-pairing mode ([Figure S4O](#)). Collectively, these observations suggest that the ability of rU-dG (and likely rG-dT) mismatches to form wobble base-pairing interactions is determined not only by backbone constraints at the specific position within the gRNA-TS DNA heteroduplex ([Figure S3F](#)) but also by local sequence context and/or the presence of neighboring mismatches ([Figures S4C–S4G](#)).

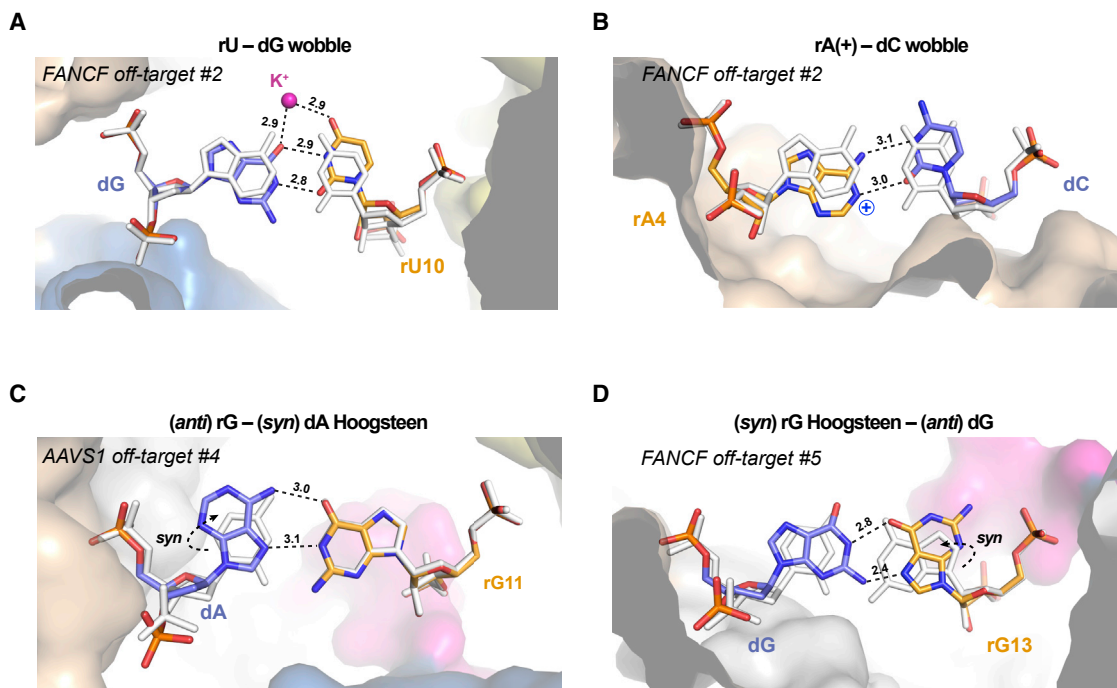


Figure 2. Cas9 off-target binding is enabled by noncanonical base pairing

(A–D) Close-up views of (A) rU–dG wobble base pair at duplex position 10 in *FANCF* off-target #2 complex, (B) rA–dC wobble base pair at position 4 in *FANCF* off-target #2 complex, (C) rG–dA Hoogsteen base pair at duplex position 11 in *AAVS1* off-target #4 complex, and (D) rG–dG Hoogsteen base pair at duplex position 13 in *FANCF* off-target #5 complex. Hydrogen-bonding interactions are indicated with dashed lines. Numbers indicate interatomic distances in Å. Corresponding on-target base pairs are shown in white. Dashed arrows indicate *anti-syn* isomerization of the dA and rG bases to enable Hoogsteen-edge base pairing. A bound monovalent ion, modeled as K⁺, is depicted as a purple sphere. See also Figure S4.

rA–dC or rC–dA mismatches can also form wobble-like base pairs when the adenine base is protonated at the N1 position (Garg and Heinemann, 2018; Wang et al., 2011). In the rA–dC mismatch found at duplex position 4, the dC base undergoes a wobble displacement compatible with the formation of two hydrogen bonds with the adenine base, indicative of adenine protonation (Figures 2B and S4P). At other duplex positions in our dataset, the rA–dC or rC–dA mismatches are instead accommodated by slight displacements of the adenine base within the base pair plane resulting in the formation of a single hydrogen bond in each case (Figures S4Q–S4S).

Accommodating purine–purine mismatches by Watson–Crick-like interactions would normally require severe distortion of the guide:off-target duplex to increase its width by more than 2 Å (Leontis et al., 2002). At positions where the duplex width is constrained by Cas9 interactions (Figure S3F), rG–dA and rA–dG mismatches are accommodated by *anti*-to-*syn* isomerization of the adenine base to form two hydrogen-bonding interactions via its Hoogsteen base edge. This is observed at duplex position 11 in the *AAVS1* off-target #4 complex (rG–dA mismatch) (Figure 2C) and at position 7 in the *AAVS1* off-target #2 complex (rA–dG mismatch) (Figure S4T). Similarly, the rG–dG mismatch at duplex position 13 in the *FANCF* off-target #5 complex is accommodated by Hoogsteen base pairing as a result by *anti*-to-*syn* isomerization of the gRNA base (Figure 2D). Overall, the observed Hoogsteen base-pairing interactions are near-isos-

teric with canonical base pairs and maintain duplex width without excessive backbone distortion (Table S4).

Duplex backbone rearrangements accommodate otherwise nonproductive mismatches

Whereas wobble (G–U/T or A–C) and Hoogsteen (A–G or G–G) base pairs are generally compatible with the canonical A-form geometry of an RNA–DNA duplex, other nucleotide mismatches only form nonisosteric base pairs that require considerable distortion of the (deoxy)ribose–phosphate backbone. The formation of pyrimidine–pyrimidine base pairs is expected to occur by a substantial reduction in duplex width (Leontis et al., 2002). This is observed at the rU–dC mismatch at duplex position 9 in the *FANCF* off-target #1 complex (Figure 3A). Here, the gRNA backbone is able to shift toward the target DNA strand, resulting in a reduction of the C1′–C1′ distance to 8.65 Å compared with 10.0 Å in the *FANCF* on-target complex. This facilitates the formation of two hydrogen-bonding interactions within the rU–dC base pair, which is further enabled by a substantial increase in base propeller twist (Figure 3A). In contrast, rC–dT mismatches remain unpaired at duplex positions 6 and 7 in Figures S5A and S5B or form only a single hydrogen bond at position 8 (Figure S5C), likely due to backbone steric constraints at these positions imposed by Cas9 interactions (Figure S3F). Backbone steric constraints also likely influence the formation of rU–dT base pairs (Figure S3F). At duplex position 7, the mismatch remains

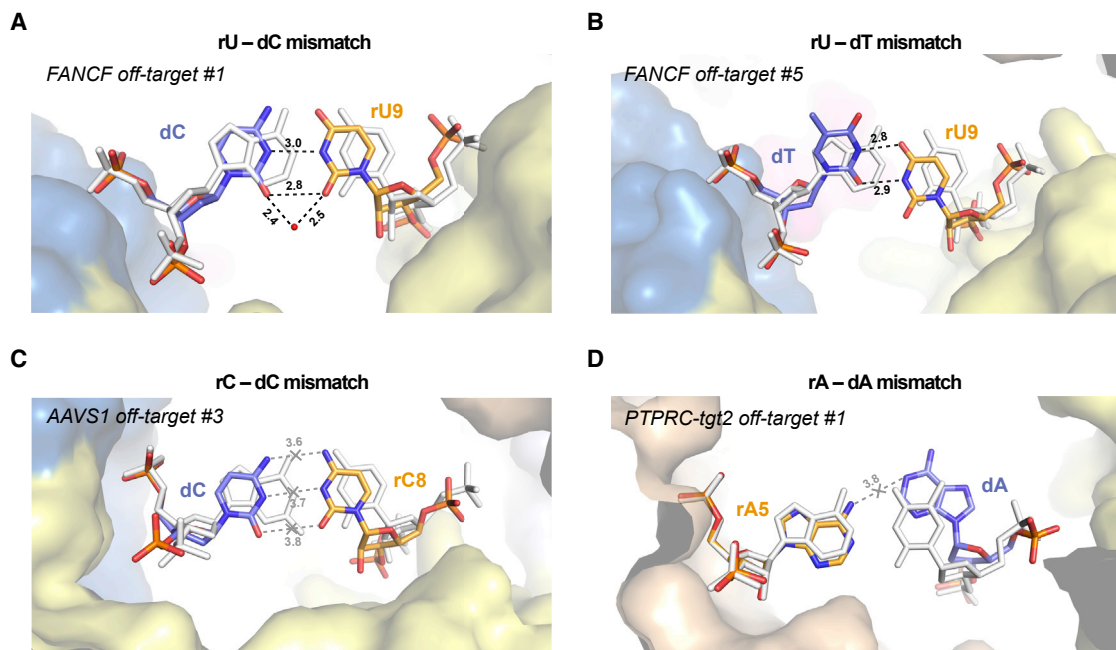


Figure 3. Duplex backbone distortions facilitate formation of noncanonical base pairs

(A–D) Close-up views of (A) rU–dC base pair at duplex position 9 in *FANCF* off-target #1 complex, (B) rU–dT base pair at position 9 in *FANCF* off-target #5 complex, (C) rC–dC mismatch at duplex position 8 in *AAVS1* off-target #3 complex, and (D) rA–dA mismatch at duplex position 5 in *PTPRC-tgt2* off-target #1 complex. Hydrogen-bonding interactions are indicated with black dashed lines. Crossed-out gray lines indicate lack of hydrogen bonding. Corresponding on-target base pairs are overlaid and colored white (for *PTPRC-tgt2*, the *FANCF* on-target structure was used and bases were mutated *in silico*). Numbers indicate interatomic distances in Å. Bound water molecule is depicted as red sphere. See also [Figures S5](#) and [S6](#).

unpaired ([Figure S5D](#)), whereas productive pairing is seen at duplex positions 8 and 9, facilitated by distortions of the gRNA and TS backbone, respectively ([Figures 3B](#), [S5E](#), and [S5F](#)). Of note, the *FANCF* off-target #7 rC–dT mismatch is bridged by hydrogen-bonding interactions with the side chain of Arg895 inserted into the minor groove of the heteroduplex ([Figure S5B](#)); however, the interaction is not essential for the tolerance of rC–dT mismatches at this position ([Figure S5G](#); [Table S5](#)).

rC–dC mismatches only form productive hydrogen-bonding interactions if bridged by a water molecule or when one of the cytosine bases is protonated ([Leontis et al., 2002](#)). Only the former is observed in the determined structures, at duplex position 5 in the *AAVS1* off-target #2 complex ([Figure S5H](#)). In contrast, at duplex positions 8 and 15, the bases remain unpaired while maintaining intrastrand base stacking interactions ([Figures 3C](#) and [S5I](#)). Similarly, rA–dA mismatches are unable to form productive hydrogen-bonding interactions within the constraints of an A-form duplex ([Leontis et al., 2002](#)). Accordingly, the rA–dA mismatch at duplex position 5, where duplex width is constrained by Cas9 ([Figure S3F](#)), is accommodated by extrusion of the dA nucleobase out of the base stack into the major groove of the duplex ([Figure 3D](#)), which is enabled by local distortion of the TS backbone ([Figure S6A](#)).

To gain further insights into the mechanism of rA–dA mismatch accommodation and extrapolate our structural observations to

other heteroduplex positions, we performed molecular dynamics (MD) simulations by introducing single rA–dA mismatches at all 20 positions along the heteroduplex in the context of the catalytically active state of Cas9 (PDB: 6O0Y) and compared the resulting trajectories with the corresponding on-target system. In-depth analysis of the rA–dA conformational dynamics was performed by computing the geometrical descriptors defining the base pair complementarity along the heteroduplex ([Figures S6B–S6G](#)) ([Lavery et al., 2009](#)). These reveal that at all positions, the rA–dA mismatch is primarily accommodated by base extrusion from the duplex, with positions 3, 5, 15, 16, 18, 19, and 20 undergoing dA base extrusion and positions 10 and 17 rA base extrusion. Notably, at duplex positions 2, 4, 6, 8, 11, and 12, the broad or bimodal distributions of base pair shear and opening parameters are indicative of considerable conformational dynamics, allowing the rA–dA mismatch to be accommodated by either rA or dA base extrusion ([Figure S6B](#)). Importantly, rA–dA mismatch simulations at positions 5, 18, and 19 showed very good agreement with the determined crystal structures (*PTPRC-tgt2* off-target #1, *FANCF* off-target #6, *AAVS1* off-target #2), predicting both dA base extrusion and backbone distortions ([Figures S6A](#) and [S6H](#)).

Analysis of our SITE-Seq assay dataset revealed that off-target rA–dA mismatches occur at all positions within the gRNA–TS DNA heteroduplex ([Figure S6I](#)), in agreement with MD simulations, as well as previous studies ([Boyle et al., 2017, 2021](#); [Doench et al., 2016](#); [Jones et al., 2021](#); [Zhang et al.,](#)

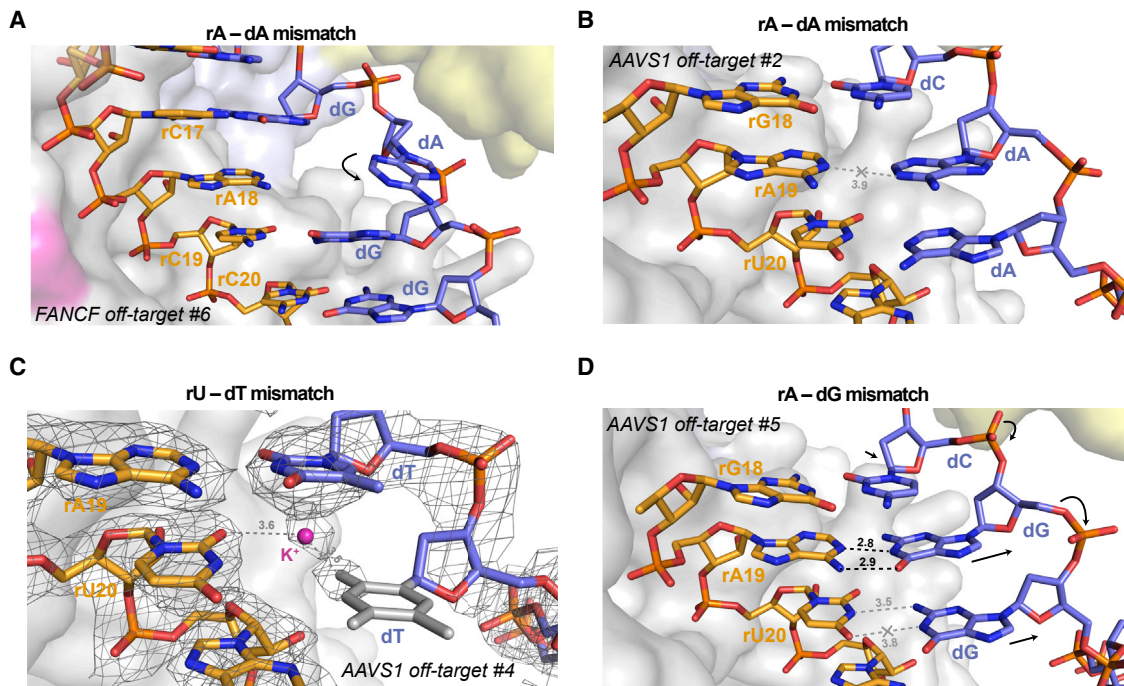


Figure 4. TS distortion facilitates mismatch accommodation in the seed region of the guide:off-target heteroduplex

(A–C) Close up views of (A) rA–dA mismatch at position 18 in *FANCF* off-target #6 complex, showing major groove extrusion of the dA base, (B) rA–dA mismatch at position 19 in *AAVS1* off-target #2 complex, showing retention of the dA base in the duplex stack, and (C) rA–dG base pair at position 19 and the unpaired rU–dG mismatch at position 20 in the *AAVS1* off-target #5 complex. (D) Close-up view of the rU–dT mismatch at the PAM-proximal position 20 in *AAVS1* off-target #4 complex. Residual electron density indicates the presence of an ion or solvent molecule. Refined $2mF_o - mF_c$ electron density map of the heteroduplex, contoured at 1.5σ , is rendered as a gray mesh. Structurally disordered thymine nucleobase for which no unambiguous density is present is in gray. Arrows indicate conformational changes in the TS backbone relative to the on-target complex.

See also Figures S6 and S7.

2020). This suggests that rA–dA mismatches do not encounter steric barriers within Cas9 that would disfavor their presence, which is consistent with the absence of specific contacts with Cas9 along the length of the major groove of the heteroduplex (Figure S3F).

PAM-proximal mismatches are accommodated by TS distortion due to seed sequence rigidity

The seed sequence of the gRNA (nucleotides 11–20) makes extensive interactions with Cas9, both in the absence and presence of bound DNA (Anders et al., 2014; Jiang et al., 2015; Nishimasu et al., 2014; Zhu et al., 2019). Structural preordering of the seed sequence by Cas9 facilitates target DNA binding and contributes to the specificity of on-target DNA recognition (Jiang et al., 2015; O’Geen et al., 2015; Wu et al., 2014). Conversely, binding of off-target DNAs containing PAM-proximal mismatches is inhibited and results in accelerated off-target dissociation (Boyle et al., 2017, 2021; Ivanov et al., 2020; Jones et al., 2021; Singh et al., 2016; Zhang et al., 2020). Nevertheless, Cas9 does tolerate most base mismatch types within the seed region of the gRNA, leading to detectable off-target DNA cleavage (Boyle et al., 2021; Doench et al., 2016; Jones et al., 2021; Zhang et al., 2020). In particular, the first two PAM-proximal positions display a markedly higher tolerance for mismatches than

the rest of the seed region (Cofsky et al., 2022; Doench et al., 2016; Hsu et al., 2013; Mekler et al., 2017; Zeng et al., 2018); this is supported by our SITE-Seq assay data as the frequency of mismatches at PAM-proximal positions 18–20 is 1.4–2.0F0B4 higher than at seed positions 14–17 (Figures S1D and S1E).

Unlike the seed region of the gRNA, the complementary PAM-proximal TS nucleotides are not directly contacted by Cas9 in the precleavage state and are thus under fewer steric constraints (Figure S3F), with the exception of duplex position 20 in which the phosphodiester group of the TS nucleotide makes extensive interactions with the phosphate-lock loop of Cas9 (Anders et al., 2014) (Figure S7A). In agreement with this, four of our off-target complex structures reveal that PAM-proximal base mismatches are accommodated solely by structural distortions of the TS backbone (Figure 4), while the conformation of the gRNA backbone and base stacking within the seed region remain unperturbed (Figures S7B and S7C). The presence of an rA–dA mismatch in the PAM-proximal position 18 results in the extrusion of the TS nucleobase into the major groove (Figure 4A), likely due to steric constraints on duplex width at this position. In contrast, the rA–dA mismatch at duplex position 19 is instead accommodated by a marked distortion in the TS backbone that results in increased duplex width, which preserves base

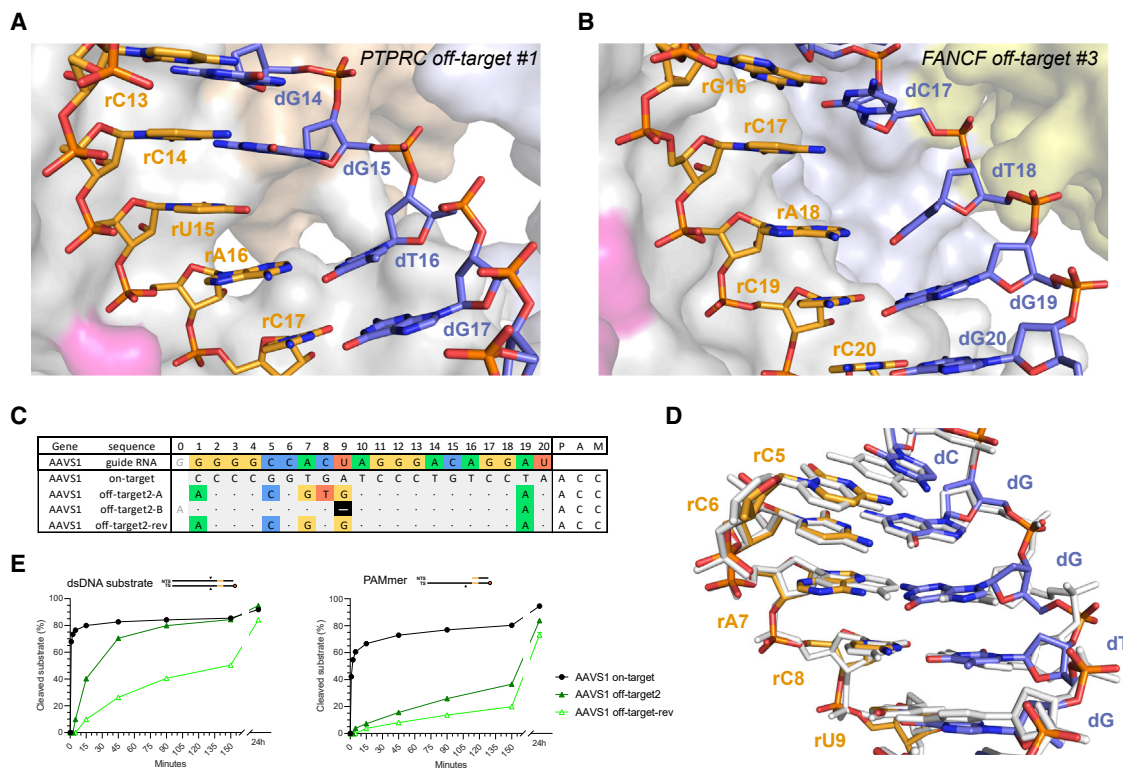


Figure 5. Off-targets with single-nucleotide deletions are accommodated by base skipping or multiple mismatches

(A) Zoomed-in view of the base skip at duplex position 15 in the *PTPRC-tgt2* off-target #1 complex.

(B) Zoomed-in view of the base skip at duplex position 17 in the *FANCF* off-target #3 complex.

(C) Schematic depiction of alternative base-pairing modes in the AAVS1 off-target #2 complex (off-target2-A and off-target2-B). AAVS1 off-target #2-rev substrate was designed based on the AAVS1 off-target #2, with the reversal of a single mismatch in the consecutive region back to the corresponding canonical base pair.

(D) Structural overlay of the AAVS1 off-target #2 (colored) and AAVS1 on-target (white) heteroduplexes.

(E) Cleavage kinetics of AAVS1 on-target, off-target #2, and off-target #2-rev DNA substrates.

See also Figures S1, S7, and S8.

stacking within the duplex in the absence of productive pairing between the adenine bases (Figures 4B and S7B). Similarly, the rA-dG mismatch at position 19 is accommodated by an ~ 2 Å displacement of the TS backbone, increasing duplex width. This not only preserves base stacking but also facilitates rA-dG base pairing by two hydrogen-bonding interactions via their Watson-Crick edges (Figures 4C and S7C). This off-target complex also contains an rU-dG mismatch at duplex position 20, which does not undergo wobble base pairing as the rU20 nucleotide is extensively contacted by Cas9 (Figure S3F) and unable to shift toward the major groove and is instead accommodated by a slight shift in the dG nucleotide (Figure 4C). Finally, the rU-dT base mismatch at duplex position 20 in the AAVS1 off-target #4 complex remains unpaired and the dT base lacks ordered electron density (Figure 4D). This is likely a result of the dT nucleotide maintaining contact with the phosphate-lock loop of Cas9 (Figure S7A), which prevents a reduction in the duplex width and precludes productive base pairing. Overall, these observations indicate that off-target DNAs containing mismatches to the seed sequence of the gRNA can be accommodated by Cas9 due to limited interactions with the TS DNA in the seed-binding region.

Cas9 recognizes off-targets with single-nucleotide deletions by base skipping or via multiple mismatches

A substantial fraction of off-target sites recovered in our SITE-Seq assay analysis (46.4%, when not considering the possibility of nucleotide insertions or deletions) contained six or more mismatched bases to the gRNA (Figure S1C; Table S1). Such off-target sequences have previously been proposed to be accommodated by bulging out or skipping of nucleotides (Boyle et al., 2021; Cameron et al., 2017; Doench et al., 2016; Jones et al., 2021; Lin et al., 2014; Tsai et al., 2015), which would result in a shift of the nucleotide register to re-establish correct base-pairing downstream of the initially encountered mismatch (Figure S1F). The *PTPRC-tgt2* off-target #1 and *FANCF* off-target #3 sites are predicted to contain single-nucleotide deletions at duplex positions 15 and 17, respectively (Figures 1A, S1F, and S1I; Table S1). The structures of the corresponding off-target complexes reveal that the single-nucleotide deletions in these off-target substrates are not accommodated by bulging out the unpaired gRNA nucleotide. Instead, the conformations of the gRNAs remain largely unperturbed and the off-target TS DNAs “skip over” the unpaired gRNA bases to resume productive base-pairing downstream (Figures 5A and 5B). The seed regions

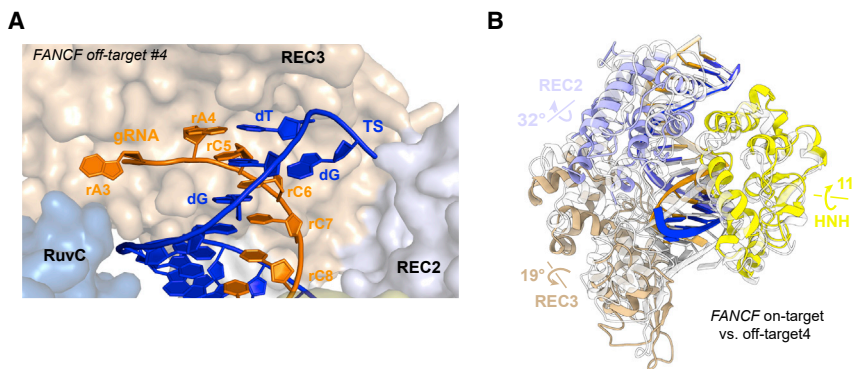


Figure 6. Cas9 conformational rearrangement upon mismatch-induced unpairing of the PAM-distal heteroduplex

(A) Close-up view of the unpairing of mismatched bases at the PAM-distal end of the *FANCF* off-target #4 heteroduplex. The last two nucleotides on each strand could not be modeled due to structural disorder.

(B) Overlay of the *FANCF* off-target #4 and *FANCF* on-target complex structures. The *FANCF* off-target #4 complex is colored according to the domain legend in Figure 1A, *FANCF* on-target complex is shown in white. The REC1, RuvC, and PAM-interaction domains have been omitted for clarity, as no structural differences are observed. See also Figure S9.

of the gRNAs make extensive interactions with the bridge helix and the REC1 domain, whereas the TS DNA backbones are displaced by almost 3 Å (Figures S7D and S7E). The base pair skips are accommodated by considerable buckling and tilting of the base pairs immediately downstream of the skip site (Table S4). An additional consequence of the base-pairing register shift is the formation of noncanonical base pairs between the off-target DNA and the extra 5'-terminal guanine nucleotides present in the gRNA as a consequence of *in vitro* transcription by T7 RNA polymerase (Figures S7F and S7G). This potentially explains the impact of the 5'-guanines on both R-loop stability and *in vitro* cleavage activity (Kulcsár et al., 2020; Mullally et al., 2020; Okafor et al., 2019).

Originally, our SITE-Seq assay analysis classified the AAVS1 off-target #2 as a single-nucleotide deletion at duplex position 9 (Figures 5C and S11; Table S1). Unexpectedly, the structure of the AAVS1 off-target #2 complex instead reveals that the off-target substrate is bound in the unshifted register, resulting in the formation of five base mismatches in the PAM-distal half of the gRNA-TS duplex (Figure 5D), including a partially paired rC-dC mismatch at position 5, an rA-dG Hoogsteen pair at position 7, a partially paired rC-dT mismatch at position 8, and a tautomeric rU-dG pair at position 9. The backbone conformations of the gRNA and the off-target TS exhibit minimal distortions and are nearly identical with the corresponding on-target heteroduplex (Figure 5D). This implies that some mismatch combinations might synergistically result in gRNA and TS backbone geometries that mimic the on-target conformation and result in off-target tolerance. To test this hypothesis, we reverted the rC-dT mismatch at position 8 to the on-target rC-dG pair, thereby reducing the total amount of off-target mismatches from 6 to 5 (Figure 5C). The resulting off-target substrate (AAVS1 off-target #2-rev) exhibited substantially reduced cleavage rates in both dsDNA and PAMmer formats, as well as a significantly increased dissociation rate (Figure 5E; Table S5). We replicated these results for two other AAVS1 off-target substrates with different mismatch patterns that were initially predicted to contain PAM-distal deletions (Figures S8A–S8C; Table S5). Together, these results suggest that some bona fide off-target substrates contain multiple consecutive mismatches, and the reversal of one mismatch may affect the structural integrity of the gRNA-TS DNA heteroduplex and interfere with DNA

binding and/or conformational activation of Cas9 despite a reduction in the total number of mismatches.

To further investigate the accommodation of PAM-distal deletions in Cas9 off-target sites, we selected an additional efficiently cleaved off-target substrate (*CD34* off-target #9; Figures S8D–S8F), containing a dT substitution at position 17 (resulting in an rU-dT mismatch with the *CD34* sgRNA) and a predicted single-nucleotide deletion at position 6. Crystal structure of the resulting complex revealed that the rU-dT mismatch involves the *syn* conformer of the rU17 nucleotide (Figure S8G). The deletion at position 6 is accommodated by base skipping, leaving the base of rA6 unpaired within the guide-TS heteroduplex stack (Figure S8H), and the register shift results enable the 5'-terminal guanine nucleotide of the gRNA (introduced during *in vitro* transcription) to base pair with 3'-terminal TS nucleotide (Figure S8I). The backbone distortions in the TS are accompanied by compensatory rearrangements of the REC2 and REC3 domains of Cas9 (Figure S8J), which preserve all contacts with the heteroduplex (Figure S3F).

Collectively, these results indicate that deletion-containing off-target complexes (Figure S11; Table S1) are accommodated either by RNA base skipping, as opposed to RNA nucleotide bulging, or by the formation of multiple base mismatches, with the precise mechanism dependent in part on the position of the deletion.

PAM-distal mismatches perturb the Cas9 conformational checkpoint

FANCF off-target #4, which contains three PAM-distal mismatches at positions 1–3 and a G-U mismatch at position 10 (Figure 1A), is reproducibly the top ranking off-target site for the *FANCF* gRNA, as detected by SITE-Seq assay analysis at the lowest Cas9 RNP concentrations (Table S1). The off-target substrate exhibits slow cleavage kinetics *in vitro* with both dsDNA and PAMmer substrates (Table 1; Figures S2A and S2B), indicating a perturbation of the conformational activation checkpoint of Cas9. The structure of the *FANCF* off-target #4 complex reveals that the RNA-DNA heteroduplex is unpaired at positions 1–3 as a result of the PAM-distal mismatches, with nucleotides 1–2 of the gRNA and 19–20 of the TS disordered (Figure 6A). Furthermore, Cas9 undergoes structural rearrangements of its REC lobe and the HNH domain (Figure 6B; Video

S2), resulting in a root-mean-square displacement of the REC2 and REC3 domains of 3.7 Å (1,315 C α atoms) relative to the *FANCF* on-target complex structure. The REC3 domain undergoes a 19-degree rotation (Figure 6B), facilitated by extending the helix comprising residues 703–712 through restructuring of loop residues 713–716 (Figure S9A), to accommodate the altered gRNA conformation. The REC2 domain rotates 32° away from the REC3 domain (Figure 6B). This is accompanied by restructuring of the hinge loop residues 174–180 and disordering of loops 258–264, 284–285, and 307–309. Concomitantly, the HNH domain rotates 11° away from the heteroduplex, compared with the *FANCF* on-target structure, to accommodate distortion of the TS DNA (Figure 6B).

The unpaired 5' end of the sgRNA is located at the interface between the REC3 and the RuvC domain and maintains interactions with heteroduplex-sensing residues Lys510, Tyr515, and Arg661 of the REC3 domain (Figures 6A and S9B). In contrast to the corresponding on-target complex structure, the unpaired 3' end of the off-target TS breaks away from the REC3 lobe and instead points toward the REC2 domain, forming unique interactions with Arg895, Asn899, Arg905, Arg919, and His930 in the HNH domain (Figure S9C). These interactions (Figure S9D) could be responsible for the observed repositioning of the REC lobe and HNH domain, and they may impede the formation of a cleavage-competent complex.

The conformation of the *FANCF* off-target #4 complex is distinct from the conformations observed in cryo-EM reconstructions of the pre- and post-cleavage states of the Cas9 complex (Zhu et al., 2019) (Figures S9E and S9F). Instead, the off-target complex structure most closely resembles that of a high-fidelity variant xCas9 3.7 containing amino acid substitutions that disrupt interactions with the TS DNA (Guo et al., 2019). Although the xCas9 3.7 complex adopts a slightly different REC lobe conformation (Figure S9G), the PAM-distal duplex also undergoes unpairing at positions 1–3 and displays a comparable degree of structural disorder (Figure S9H). These structural observations thus suggest that the presence of multiple mismatches in the PAM-distal region of a gRNA-off-target DNA duplex leads to conformational perturbations in the DNA-bound complex that resemble the structural consequences of specificity-enhancing mutations in high-fidelity Cas9 variants.

DISCUSSION

The off-target activity of Cas9 has been extensively documented in prior genome editing, biochemical and biophysical studies (Boyle et al., 2017; Boyle et al., 2021; Doench et al., 2016; Jones et al., 2021; Lazzarotto et al., 2020; Zhang et al., 2020). Although numerous methods have been devised for computational prediction of genomic off-target sites and their experimental validation, these have reported highly variable mismatch tolerance profiles depending on the screening method and the target sequence. Thus, a comprehensive understanding of this phenomenon is still lacking. In this study, we used the SITE-Seq assay to examine the off-target landscape of 12 well-studied gRNAs, observing a broad variation of cleavage activities associated with individual off-target substrates. To shed light on the molecular mechanisms underlying off-target activity, we deter-

mined atomic structures of a representative set of 16 off-target complexes, providing fundamental insights into the structural aspects of off-target recognition.

Role of noncanonical base pairing in off-target recognition

The principal, and largely unexpected, finding of our structural analysis is that the majority of nucleotide mismatches in bona fide off-target substrates are accommodated by noncanonical base-pairing interactions. These range from simple wobble or Hoogsteen base-pairing interactions to pyrimidine-pyrimidine pairs that rely on (deoxy)ribose-phosphate backbone distortions that reduce duplex width. With the notable exception of rA-dA mismatches, which are accommodated by extrahelical base extrusion, the structural rearrangements associated with base mismatch accommodation largely preserve base stacking, which is the primary determinant of nucleic acid duplex stability (Yakovchuk et al., 2006). For some off-target sequences, our structures are suggestive of base protonation or tautomerization facilitating hydrogen-bonding interactions in otherwise nonpermissive mismatches, such as rA-dC. These rare base pair forms have been previously observed in both RNA and DNA duplexes and are thought to be important contributors to DNA replication and translation errors (Kimsey et al., 2015, 2018). Future studies employing complementary structural methods, such as nuclear magnetic resonance, will help confirm the occurrence of noncanonical base states in off-target complexes.

The mismatch tolerance of Cas9 can be explained primarily by two factors. First, Cas9 does not directly contact the major- or minor-groove edges of the gRNA-TS DNA heteroduplex base pairs at any of the duplex positions and thus lacks a steric mechanism to enforce Watson-Crick base pairing. This is further underscored by Cas9's tolerance of base modifications in target DNA, including cytosine 5-hydroxymethylation and, at least at some duplex positions, glucosyl-5-hydroxymethylation (Vlot et al., 2018). In this respect, Cas9 differs from other molecular systems, notably the ribosome and replicative DNA polymerases, which enhance the specificity of base pairing by direct readout of base-pair shape and steric rejection of mismatches (Kunkel and Bebenek, 2000; Rodnina and Wintermeyer, 2001; Timsit, 1999).

Second, Cas9 is a multidomain protein that displays considerable conformational plasticity and is therefore able to accommodate local distortions in the guide-TS duplex geometry by compensatory rearrangements of the REC2, REC3, and HNH domains (Chen et al., 2017; Donohoue et al., 2021). Indeed, in most off-target structures reported in this study, almost all atomic contacts between Cas9 and the guide-TS heteroduplex are preserved. Thus, Cas9 only detects guide-target mismatches by indirect readout of the gRNA-TS DNA heteroduplex width, except at the PAM-distal end of the heteroduplex where base mismatches result in duplex unpairing, as discussed below. Our observations are consistent with recent MD simulation studies showing that internally positioned mismatches within the gRNA-TS DNA heteroduplex are readily incorporated within the heteroduplex and have only minor effects on Cas9 interactions (Mitchell et al., 2020). The lack of a steric base pair enforcement mechanism and the resulting off-target promiscuity

likely reflects the biological function of Cas9 in CRISPR immunity, enabling targeting of closely related viruses and hindering immune evasion by mutations or covalent base modifications (Deveau et al., 2008; Semenova et al., 2011; van Houte et al., 2016; Yaung et al., 2014). On the other hand, such conformational plasticity also enables the incorporation of various chemical modifications in the gRNA that are compatible with the A-form geometry of the heteroduplex (Cromwell et al., 2018; Donohoue et al., 2021; Hendel et al., 2015; O'Reilly et al., 2019; Yin et al., 2018, 2017). These could potentially disfavor the formation of certain noncanonical base pairs or reduce the backbone flexibility of the gRNA, thereby enhancing off-target discrimination. However, the effect of specific gRNA modifications on particular types of mismatches is yet to be closely examined mechanistically (Donohoue et al., 2021).

Importance of guide RNA seed sequence for off-target discrimination

The seed sequence of the Cas9 gRNA (nucleotides 11–20) is the primary determinant of target DNA binding, a consequence of its structural preordering in an A-like conformation by extensive interactions with Cas9 (Anders et al., 2014; Jiang et al., 2015; Nishimasu et al., 2014; Zhu et al., 2019). Our data indicate that structural rigidity of the gRNA seed sequence also affects off-target recognition, as base mismatches in the seed region of the heteroduplex can only be accommodated by conformational distortions of TS DNA, which is subject to only a few steric constraints, notably at position 20 due to interactions with the phosphate-lock loop (Anders et al., 2014). This increases the energetic penalty of base mispairing in the seed region of the heteroduplex and thus contributes to mismatch sensitivity of Cas9 within the seed region. Although structural distortions of TS DNA facilitate binding of off-target substrates containing seed mismatches, they may nevertheless inhibit off-target cleavage by steric hindrance of the HNH domain, thereby further contributing to off-target discrimination. The contrasting structural plasticities of the gRNA and TS DNA strands are manifested in the differential activities of Cas9 against off-targets containing rU-dG and rG-dT mismatches within the seed region (Boyle et al., 2021; Doench et al., 2016; Hsu et al., 2013; Jones et al., 2021; Zhang et al., 2020). Whereas rG-dT mismatches can be readily accommodated by wobble base pairing, seed sequence rigidity is expected to hinder rU-dG wobble base pairing. Combined with a lower energetic penalty associated with rG-dT mismatch binding (binding an off-target with an rG-dT mismatch requires unpairing a dT-dA base pair in the off-target DNA, while rU-dG off-target recognition requires dC-dG unpairing), these effects thus help Cas9 discriminate against rU-dG mismatches in the seed region.

Recognition of off-targets containing insertions and deletions

Bona fide off-target sites containing insertions or deletions have been detected in a number of studies (Boyle et al., 2021; Cameron et al., 2017; Doench et al., 2016; Jones et al., 2021; Tsai et al., 2015). Nucleotide “bulging” has been proposed as a mechanism to recognize such off-targets, which would otherwise result in large numbers of consecutive base mismatches. However, as Cas9 encloses the gRNA-TS DNA heteroduplex in

a central channel and makes extensive interactions along the entire length of the gRNA strand, the formation of RNA bulges is precluded by steric clashes, pointing to a different mechanism.

Indeed, our structural analysis provides no evidence for RNA bulging. Instead, the structures of *PTPRC-tgt2* off-target #1 and *FANCF* off-target #3 complexes reveal that off-target sequences predicted to contain single-nucleotide deletions in the seed region of the heteroduplex are recognized by base skipping, resulting in an unpaired gRNA base within the duplex stack, incurring a large energetic penalty. This is enabled by the lack of extensive contacts of Cas9 with the TS, while rigid coordination of the gRNA in the seed region disfavors extrahelical guide RNA bulging. As the seed region of the TS DNA is devoid of Cas9 contacts in the gRNA precleavage state (Zhu et al., 2019), off-targets containing single-nucleotide insertions in the seed region of the heteroduplex are likely to be recognized by DNA nucleotide bulging, likewise incurring a large energetic penalty as unwinding an off-target DNA sequence containing an insertion requires breaking an extra base pair. Moreover, TS DNA distortion might inhibit cleavage by steric hindrance of the HNH domain.

In contrast, off-target sequences containing deletions in the PAM-distal region of the heteroduplex (positions 1–10) can be recognized either by base skipping, as in the case of *CD34* off-target #9, or bound in the unshifted register, with multiple base mismatches accommodated by noncanonical base-pairing interactions, as seen for *AAVS1* off-target #2, which was previously predicted to contain an RNA bulge or skip (Cameron et al., 2017; Lazzarotto et al., 2020). Which of the two mechanisms is used likely depends on the off-target sequence and the position of the deletion, which in turn dictate the number of mismatches between the guide and the off-target sequence in the unshifted register. Off-target accommodation by multiple noncanonical base pairs likely relies on their synergistic effect to mimic the on-target heteroduplex geometry, which enables unperturbed binding, as supported by our observations that mismatch reversal in several off-target substrates reduces their rates of cleavage. Although our structural analysis does not examine off-target substrates containing insertions, we posit that PAM-distal insertions are recognized as multiple mismatches due to steric hindrance of extrahelical bulging. Thus, our structural findings suggest that a substantial fraction of off-target sites predicted to contain insertions or deletions may be bound via multiple mismatches instead (Boyle et al., 2021; Doench et al., 2016; Jones et al., 2021). Furthermore, these observations explain why Cas9 appears to tolerate mismatches better than insertions or deletions and why deletions and insertions within the seed region are particularly deleterious (Boyle et al., 2021; Cameron et al., 2017; Doench et al., 2016; Jones et al., 2021).

PAM-distal base pairing and the conformational checkpoint of Cas9

Upon substrate DNA hybridization and R-loop formation, Cas9 undergoes conformational activation of its nuclease domains (Bravo et al., 2022; Pacesa et al., 2022; Zhu et al., 2019). The Cas9 REC3 domain plays a key role in the process, as it senses the integrity of the PAM-distal region of the gRNA-TS DNA heteroduplex and allosterically regulates the REC2 and HNH

domains, providing a conformational checkpoint that traps Cas9 in a conformationally inactive state in the absence of PAM-distal hybridization (Chen et al., 2017; Dagdas et al., 2017; Palermo et al., 2018; Zhu et al., 2019). Our structural data confirm that mismatches at the PAM-distal end of the heteroduplex (positions 1–3) result in heteroduplex unpairing, incomplete R-loop formation, and structural repositioning of the REC3 domain (Figure 6), indicating a perturbation of the Cas9 conformational checkpoint. We envision that the observed conformational state mimics the structural effect of 5'-truncated gRNAs, which have been shown to improve targeting specificity (Fu et al., 2014). Furthermore, similarities with the structure of a high-fidelity Cas9 variant (Guo et al., 2019) suggest a shared underlying mechanism for increased specificity.

Implications for off-target prediction

Our structural data reveal that Cas9 plays a limited steric role in off-target discrimination insofar as only sensing the integrity and general shape of the guide-target heteroduplex. Off-target activity is thus largely determined by the kinetics and energetics of R-loop formation, that is off-target DNA strand separation and concomitant gRNA-TS DNA hybridization, and subsequent Cas9 conformational activation. We observe on multiple occasions that a given mismatch adopts different conformational arrangements depending on its position along the gRNA-TS DNA heteroduplex, as further supported by MD simulations of rA-dA mismatches. This poses a challenge for *ab initio* modeling of off-target activity, as biophysical models of off-target binding and cleavage are bound to be of limited accuracy unless they incorporate position-dependent energetic penalties for each base mismatch type and for deletions, as well as position- and base-specific penalties for insertions (Boyle et al., 2021; Jones et al., 2021; Zhang et al., 2020). As illustrated by our study, MD simulations can complement experimental data to provide structural information on specific mismatches at the remaining positions within the heteroduplex. Thus, ongoing structural and computational studies, combined with machine learning approaches, will assist in generating complete models for off-target prediction.

Furthermore, as certain off-target sequences that are incompatible with dsDNA cleavage can undergo NTS nicking (Fu et al., 2019; Jones et al., 2021; Murugan et al., 2020; Zeng et al., 2018), future bioinformatic models need to be able to predict off-target nicking activity as well. Furthermore, accurate modeling of off-target interactions remains difficult due to context-dependent effects, as documented in previous studies showing that the binding and cleavage defects of consecutive mismatches deviate from additivity (Boyle et al., 2021; Cameron et al., 2017; Lazzarotto et al., 2020; Zhang et al., 2020). Indeed, our structural data rationalize this by showing that the conformation of a given base mismatch is highly sensitive to the presence of neighboring mismatches. As seen in the case of AAVS1 off-target #2 complex, multiple mismatched bases can synergistically combine to preserve an on-target-like heteroduplex conformation that passes the REC3 conformational checkpoint, supporting nearly on-target efficiencies of cleavage (Zhang et al., 2020). This is in line with recent cryo-EM structural studies suggesting that indirect readout of heteroduplex conformation is

coupled to nuclease activation, while mismatches disrupt this coupling (Bravo et al., 2022; Pacesa et al., 2022). Critically, reversal of one of the mismatches in this off-target substrate impairs cleavage activity. Similar effects have been described for other DNA-binding proteins such as transcription factors, where mismatches modulate transcription factor binding activity by affecting the conformation of the DNA duplex (Afek et al., 2020). In an analogy with Cas9, these proteins check for correct binding sites through indirect sequence readout by sampling for the correct duplex shape rather than base sequence (Abe et al., 2015; Kitayner et al., 2010; Rohs et al., 2009a, 2009b).

In conclusion, structural insights presented in this study establish an initial framework for understanding the molecular basis for the off-target activity of Cas9. In conjunction with ongoing computational studies, these findings will help achieve improved energetic parametrization of off-target mismatches and deletions/insertions, thus contributing to the development of more accurate off-target prediction algorithms and more specific gRNA designs. In doing so, these studies will contribute toward increasing the precision of CRISPR-Cas9 genome editing and the safety of its therapeutic applications.

Limitations of the study

The structural dataset presented in this study is necessarily restricted in scope. Although all mismatch types are covered, a much larger collection of off-target complex structures would be required to cover all mismatches at all positions to achieve a complete structural overview of the mismatch tolerance underpinning intrinsic off-target activity of Cas9. Although MD simulations can help fill in the gaps in the experimental data, our findings suggest that mismatch accommodation appears to be sequence context dependent, thus limiting their predictive power. Although we provide insights into off-target substrates containing single-nucleotide deletions, it is presently difficult to predict which mechanism occurs at a given heteroduplex position. Moreover, we currently lack structural data for off-target substrates containing insertions, which will be addressed in future studies. Finally, not all structurally characterized off-targets (~50%) are efficiently cleaved in cells, despite detectable cleavage *in vitro*, implying that additional factors affect Cas9 off-targeting in the context of eukaryotic genomes. Thus, further work combining structural and computational approaches will be needed to accurately predict the off-target activity of Cas9.

STAR★METHODS

Detailed methods are provided in the online version of this paper and include the following:

- KEY RESOURCES TABLE
- RESOURCE AVAILABILITY
 - Lead contact
 - Materials availability
 - Data and code availability
- EXPERIMENTAL MODEL AND SUBJECT DETAILS
- METHOD DETAILS
 - DNA oligonucleotides and substrates
 - Cas9 protein expression and purification

- sgRNA transcription and purification
 - Crystallization of Cas9 ternary complexes and structure determination
 - *In vitro* nuclease activity assays
 - switchSENSE analysis
 - SITE-Seq assay
 - SITE-Seq assay analysis and selection for cellular validation
 - *In silico* mismatch, deletion, and insertion classification
 - Generation of ribonucleoprotein complexes (RNP) for electroporation
 - T cell handling and nucleofection
 - Targeted amplicon sequencing
 - Molecular Dynamics (MD) simulations
- **QUANTIFICATION AND STATISTICAL ANALYSIS**

SUPPLEMENTAL INFORMATION

Supplemental information can be found online at <https://doi.org/10.1016/j.cell.2022.09.026>.

ACKNOWLEDGMENTS

We thank members of the Jinek laboratory and Caribou Biosciences, Inc. for discussion and critical reading of the manuscript. We thank Christelle Chanez and Michael Schmitz for their assistance with preparing reagents. We thank Kenny B. Jungfer for assistance with crystallographic data collection. We thank John Hawkins and Ilya Finkelstein for providing access to the NucleaSEQ prediction pipeline. We thank Vincent Olieric, Meitian Wang, and Takashi Tomizaki (Swiss Light Source, Paul Scherrer Institute) for assistance with crystallographic data collection, and Nena Matscheko from Dynamic Biosensors for support with switchSENSE experiments. We thank the NCCR RNA and Disease for providing infrastructural support. This work was supported by the Swiss National Science Foundation grant 31003A_182567 (to M.J.), the National Institutes of Health grant no. R01GM141329 (to G.P.), and the National Science Foundation grant no. CHE-1905374 (to G.P.). M.J. is an International Research Scholar of the Howard Hughes Medical Institute and Vallee Scholar of the Bert L & N Kuggie Vallee Foundation.

AUTHOR CONTRIBUTIONS

M.P., P.C., P.D.D., and M.J. conceived the study. M.P. purified wild-type Cas9, performed *in vitro* cleavage assays, crystallized ternary Cas9 complexes, solved the structures, and performed structural analysis along with M.J.; A.C. performed switchSENSE binding measurements, under the supervision of F.H.-T.A.; A.S. and P.R.A. performed MD simulations, under the supervision of G.P.; M.J.I. performed the SITE-Seq assay; C.-H.L. performed computational off-target classification, and P.D.D. and P.C. analyzed the output; K.B. purified dCas9, transcribed sgRNAs, and prepared DNA substrates for *in vitro* cleavage assays; M.P., P.C., P.D.D., and M.J. wrote the manuscript.

DECLARATION OF INTERESTS

P.D.D. is a current employee of Caribou Biosciences, Inc., and C.-H.L., M.J.I., and P.C. are former employees of Caribou Biosciences, Inc. M.J. is a cofounder of Caribou Biosciences, Inc. M.J., M.J.I., P.C., and P.D.D. are named inventors on patents and patent applications related to CRISPR-Cas technologies. SITE-Seq is a registered trademark of Caribou Biosciences, Inc.

Received: November 18, 2021

Revised: July 1, 2022

Accepted: September 15, 2022

Published: October 27, 2022

REFERENCES

- Abe, N., Dror, I., Yang, L., Slattery, M., Zhou, T., Bussemaker, H.J., Rohs, R., and Mann, R.S. (2015). Deconvolving the recognition of DNA shape from sequence. *Cell* 161, 307–318.
- Adams, P.D., Afonine, P.V., Bunkóczi, G., Chen, V.B., Davis, I.W., Echols, N., Headd, J.J., Hung, L.W., Kapral, G.J., Grosse-Kunstleve, R.W., et al. (2010). Phenix: a comprehensive Python-based system for macromolecular structure solution. *Acta Crystallogr. D Biol. Crystallogr.* 66, 213–221.
- Afek, A., Shi, H., Rangadurai, A., Sahay, H., Senitzki, A., Khani, S., Fang, M., Salinas, R., Mielko, Z., Pufall, M.A., et al. (2020). DNA mismatches reveal conformational penalties in protein-DNA recognition. *Nature* 587, 291–296.
- Anders, C., Niewoehner, O., Duerst, A., and Jinek, M. (2014). Structural basis of PAM-dependent target DNA recognition by the Cas9 endonuclease. *Nature* 513, 569–573.
- Anzalone, A.V., Koblan, L.W., and Liu, D.R. (2020). Genome editing with CRISPR-Cas nucleases, base editors, transposases and prime editors. *Nat. Biotechnol.* 38, 824–844.
- Bae, S., Park, J., and Kim, J.S. (2014). Cas-OFFinder: a fast and versatile algorithm that searches for potential off-target sites of Cas9 RNA-guided endonucleases. *Bioinformatics* 30, 1473–1475.
- Banáš, P., Hollas, D., Zgarbová, M., Jurečka, P., Orozco, M., Cheatham, T.E., 3rd, Šponer, J., and Otyepka, M. (2010). Performance of molecular mechanics force fields for RNA simulations: stability of UUCG and GNRA hairpins. *J. Chem. Theory Comput.* 6, 3836–3849.
- Berendsen, H.J.C., Postma, J.P.M., van Gunsteren, W.F.v., DiNola, A., and Haak, J.R. (1984). Molecular dynamics with coupling to an external bath. *J. Chem. Phys.* 81, 3684–3690.
- Boyle, E.A., Andreasson, J.O.L., Chircus, L.M., Sternberg, S.H., Wu, M.J., Guegler, C.K., Doudna, J.A., and Greenleaf, W.J. (2017). High-throughput biochemical profiling reveals sequence determinants of dCas9 off-target binding and unbinding. *Proc. Natl. Acad. Sci. USA* 114, 5461–5466.
- Boyle, E.A., Becker, W.R., Bai, H.B., Chen, J.S., Doudna, J.A., and Greenleaf, W.J. (2021). Quantification of Cas9 binding and cleavage across diverse guide sequences maps landscapes of target engagement. *Sci. Adv.* 7, eabe5496.
- Bravo, J.P.K., Liu, M.S., Hibshman, G.N., Dangerfield, T.L., Jung, K., McCool, R.S., Johnson, K.A., and Taylor, D.W. (2022). Structural basis for mismatch surveillance by CRISPR-Cas9. *Nature* 603, 343–347.
- Cameron, P., Fuller, C.K., Donohoue, P.D., Jones, B.N., Thompson, M.S., Carter, M.M., Gradia, S., Vidal, B., Garner, E., Slorach, E.M., et al. (2017). Mapping the genomic landscape of CRISPR-Cas9 cleavage. *Nat. Methods* 14, 600–606.
- Case, D.A., Aktulga, H.M., Belfon, K., Ben-Shalom, I.Y., Brozell, S.R., Cerutti, D.S., Cheatham, T.E., III, Cisneros, G.A., Cruzeiro, V.W.D., Darden, T.A., et al. (2021). Amber 2021 (University of California, San Francisco). <https://ambermd.org/doc12/Amber21.pdf>.
- Chen, J.S., Dagdas, Y.S., Kleinstiver, B.P., Welch, M.M., Sousa, A.A., Harrington, L.B., Sternberg, S.H., Joung, J.K., Yildiz, A., and Doudna, J.A. (2017). Enhanced proofreading governs CRISPR-Cas9 targeting accuracy. *Nature* 550, 407–410.
- Chen, V.B., Arendall, W.B., 3rd, Headd, J.J., Keedy, D.A., Immormino, R.M., Kapral, G.J., Murray, L.W., Richardson, J.S., and Richardson, D.C. (2010). MolProbity: all-atom structure validation for macromolecular crystallography. *Acta Crystallogr. D Biol. Crystallogr.* 66, 12–21.
- Cofsky, J.C., Soczek, K.M., Knott, G.J., Nogales, E., and Doudna, J.A. (2022). CRISPR-Cas9 bends and twists DNA to read its sequence. *Nat. Struct. Mol. Biol.* 29, 395–402.
- Cromwell, C.R., Sung, K., Park, J., Krysler, A.R., Jovel, J., Kim, S.K., and Hubbard, B.P. (2018). Incorporation of bridged nucleic acids into CRISPR RNAs improves Cas9 endonuclease specificity. *Nat. Commun.* 9, 1448.
- Dagdas, Y.S., Chen, J.S., Sternberg, S.H., Doudna, J.A., and Yildiz, A. (2017). A conformational checkpoint between DNA binding and cleavage by CRISPR-Cas9. *Sci. Adv.* 3, eaao0027.

- Deltcheva, E., Chylinski, K., Sharma, C.M., Gonzales, K., Chao, Y., Pirzada, Z.A., Eckert, M.R., Vogel, J., and Charpentier, E. (2011). CRISPR RNA maturation by trans-encoded small RNA and host factor RNase III. *Nature* **471**, 602–607.
- Deveau, H., Barrangou, R., Garneau, J.E., Labonté, J., Fremaux, C., Boyaval, P., Romero, D.A., Horvath, P., and Moineau, S. (2008). Phage response to CRISPR-encoded resistance in *Streptococcus thermophilus*. *J. Bacteriol.* **190**, 1390–1400.
- Doench, J.G., Fusi, N., Sullender, M., Hegde, M., Vaimberg, E.W., Donovan, K.F., Smith, I., Tothova, Z., Wilen, C., Orchard, R., et al. (2016). Optimized sgRNA design to maximize activity and minimize off-target effects of CRISPR-Cas9. *Nat. Biotechnol.* **34**, 184–191.
- Donohoue, P.D., Pacesa, M., Lau, E., Vidal, B., Irby, M.J., Nyer, D.B., Rotstein, T., Banh, L., Toh, M.S., Gibson, J., et al. (2021). Conformational control of Cas9 by CRISPR hybrid RNA-DNA guides mitigates off-target activity in T cells. *Mol. Cell* **81**. 3637.e5–3649.e5.
- Emsley, P., Lohkamp, B., Scott, W.G., and Cowtan, K. (2010). Features and development of coot. *Acta Crystallogr. D Biol. Crystallogr.* **66**, 486–501.
- Fu, B.X.H., Smith, J.D., Fuchs, R.T., Mabuchi, M., Curcuru, J., Robb, G.B., and Fire, A.Z. (2019). Target-dependent nickase activities of the CRISPR-Cas nucleases Cpf1 and Cas9. *Nat. Microbiol.* **4**, 888–897.
- Fu, Y., Sander, J.D., Reyon, D., Cascio, V.M., and Joung, J.K. (2014). Improving CRISPR-Cas nuclease specificity using truncated guide RNAs. *Nat. Biotechnol.* **32**, 279–284.
- Garg, A., and Heinemann, U. (2018). A novel form of RNA double helix based on G.U and C.A⁺ wobble base pairing. *RNA* **24**, 209–218.
- Gong, S., Yu, H.H., Johnson, K.A., and Taylor, D.W. (2018). DNA unwinding is the primary determinant of CRISPR-Cas9 activity. *Cell Rep.* **22**, 359–371.
- Guo, M., Ren, K., Zhu, Y., Tang, Z., Wang, Y., Zhang, B., and Huang, Z. (2019). Structural insights into a high fidelity variant of SpCas9. *Cell Res.* **29**, 183–192.
- Hendel, A., Bak, R.O., Clark, J.T., Kennedy, A.B., Ryan, D.E., Roy, S., Steinfeld, I., Lunstad, B.D., Kaiser, R.J., Wilkens, A.B., et al. (2015). Chemically modified guide RNAs enhance CRISPR-Cas genome editing in human primary cells. *Nat. Biotechnol.* **33**, 985–989.
- Hsu, P.D., Scott, D.A., Weinstein, J.A., Ran, F.A., Konermann, S., Agarwala, V., Li, Y., Fine, E.J., Wu, X., Shalem, O., et al. (2013). DNA targeting specificity of RNA-guided Cas9 nucleases. *Nat. Biotechnol.* **31**, 827–832.
- Ivani, I., Dans, P.D., Noy, A., Pérez, A., Faustino, I., Hospital, A., Walther, J., Andrio, P., Goñi, R., Balaceanu, A., et al. (2016). Parmbsc1: a refined force field for DNA simulations. *Nat. Methods* **13**, 55–58.
- Ivanov, I.E., Wright, A.V., Cofsky, J.C., Aris, K.D.P., Doudna, J.A., and Bryant, Z. (2020). Cas9 interrogates DNA in discrete steps modulated by mismatches and supercoiling. *Proc. Natl. Acad. Sci. USA* **117**, 5853–5860.
- Jiang, F., Taylor, D.W., Chen, J.S., Kornfeld, J.E., Zhou, K., Thompson, A.J., Nogales, E., and Doudna, J.A. (2016). Structures of a CRISPR-Cas9 R-loop complex primed for DNA cleavage. *Science* **351**, 867–871.
- Jiang, F., Zhou, K., Ma, L., Gressel, S., and Doudna, J.A. (2015). Structural biology. A Cas9-guide RNA complex preorganized for target DNA recognition. *Science* **348**, 1477–1481.
- Jinek, M., Chylinski, K., Fonfara, I., Hauer, M., Doudna, J.A., and Charpentier, E. (2012). A programmable dual-RNA-guided DNA endonuclease in adaptive bacterial immunity. *Science* **337**, 816–821.
- Jones, S.K., Jr., Hawkins, J.A., Johnson, N.V., Jung, C., Hu, K., Rybarski, J.R., Chen, J.S., Doudna, J.A., Press, W.H., and Finkelstein, I.J. (2021). Massively parallel kinetic profiling of natural and engineered CRISPR nucleases. *Nat. Biotechnol.* **39**, 84–93.
- Jorgensen, W.L., Chandrasekhar, J., Madura, J.D., Impey, R.W., and Klein, M.L. (1983). Comparison of simple potential functions for simulating liquid water. *J. Chem. Phys.* **79**, 926–935.
- Kabsch, W. (2010). XDS. *Acta Crystallogr. D Biol. Crystallogr.* **66**, 125–132.
- Kimsey, I.J., Petzold, K., Sathyamoorthy, B., Stein, Z.W., and Al-Hashimi, H.M. (2015). Visualizing transient Watson-Crick-like mispairs in DNA and RNA duplexes. *Nature* **519**, 315–320.
- Kimsey, I.J., Szymanski, E.S., Zahurancik, W.J., Shakya, A., Xue, Y., Chu, C.C., Sathyamoorthy, B., Suo, Z., and Al-Hashimi, H.M. (2018). Dynamic basis for dG⁺dT misincorporation via tautomerization and ionization. *Nature* **554**, 195–201.
- Kitayner, M., Rozenberg, H., Rohs, R., Suad, O., Rabinovich, D., Honig, B., and Shakked, Z. (2010). Diversity in DNA recognition by p53 revealed by crystal structures with Hoogsteen base pairs. *Nat. Struct. Mol. Biol.* **17**, 423–429.
- Krissinel, E., and Henrick, K. (2007). Inference of macromolecular assemblies from crystalline state. *J. Mol. Biol.* **372**, 774–797.
- Kulcsár, P.I., Tálas, A., Tóth, E., Nyeste, A., Ligeti, Z., Welker, Z., and Welker, E. (2020). Blackjack mutations improve the on-target activities of increased fidelity variants of SpCas9 with 5'G-extended sgRNAs. *Nat. Commun.* **11**, 1223.
- Kunkel, T.A., and Bebenek, K. (2000). DNA replication fidelity. *Annu. Rev. Biochem.* **69**, 497–529.
- Kuscu, C., Arslan, S., Singh, R., Thorpe, J., and Adli, M. (2014). Genome-wide analysis reveals characteristics of off-target sites bound by the Cas9 endonuclease. *Nat. Biotechnol.* **32**, 677–683.
- Lavery, R., Moakher, M., Maddocks, J.H., Petkeviciute, D., and Zakrzewska, K. (2009). Conformational analysis of nucleic acids revisited: curves+. *Nucleic Acids Res.* **37**, 5917–5929.
- Lazzarotto, C.R., Malinin, N.L., Li, Y., Zhang, R., Yang, Y., Lee, G., Cowley, E., He, Y., Lan, X., Jividen, K., et al. (2020). CHANGE-seq reveals genetic and epigenetic effects on CRISPR-Cas9 genome-wide activity. *Nat. Biotechnol.* **38**, 1317–1327.
- Leontis, N.B., Stombaugh, J., and Westhof, E. (2002). The non-Watson-Crick base pairs and their associated isostericity matrices. *Nucleic Acids Res.* **30**, 3497–3531.
- Li, P., and Merz, K.M. (2014). Taking into account the ion-induced dipole interaction in the nonbonded model of ions. *J. Chem. Theory Comput.* **10**, 289–297.
- Li, S., Olson, W.K., Lu, X.J., Li, S., Olson, W.K., and Lu, X.J. (2019). Web 3DNA 2.0 for the analysis, visualization, and modeling of 3D nucleic acid structures. *Nucleic Acids Res.* **47**, W26–W34. (2019).
- Lin, Y., Cradick, T.J., Brown, M.T., Deshmukh, H., Ranjan, P., Sarode, N., Wile, B.M., Vertino, P.M., Stewart, F.J., and Bao, G. (2014). CRISPR/Cas9 systems have off-target activity with insertions or deletions between target DNA and guide RNA sequences. *Nucleic Acids Res.* **42**, 7473–7485.
- Maier, J.A., Martinez, C., Kasavajhala, K., Wickstrom, L., Hauser, K.E., and Simmerling, C. (2015). ff14SB: improving the accuracy of protein side chain and backbone parameters from ff99SB. *J. Chem. Theory Comput.* **11**, 3696–3713.
- Makarova, K.S., Wolf, Y.I., Iranzo, J., Shmakov, S.A., Alkhnbashi, O.S., Brouns, S.J.J., Charpentier, E., Cheng, D., Haft, D.H., Horvath, P., et al. (2020). Evolutionary classification of CRISPR-Cas systems: a burst of class 2 and derived variants. *Nat. Rev. Microbiol.* **18**, 67–83.
- Mekler, V., Minakhin, L., and Severinov, K. (2017). Mechanism of duplex DNA destabilization by RNA-guided Cas9 nuclease during target interrogation. *Proc. Natl. Acad. Sci. USA* **114**, 5443–5448.
- Mitchell, B.P., Hsu, R.V., Medrano, M.A., Zewde, N.T., Narkhede, Y.B., and Palermo, G. (2020). Spontaneous embedding of DNA mismatches Within the RNA:DNA hybrid of CRISPR-Cas9. *Front. Mol. Biosci.* **7**, 39.
- Mullally, G., van Aelst, K., Naqvi, M.M., Diffin, F.M., Karvelis, T., Gasiunas, G., Siksnys, V., and Szczelkun, M.D. (2020). 5' Modifications to CRISPR-Cas9 gRNA can change the dynamics and size of R-loops and inhibit DNA cleavage. *Nucleic Acids Res.* **48**, 6811–6823.
- Murugan, K., Seetharam, A.S., Severin, A.J., and Sashital, D.G. (2020). CRISPR-Cas12a has widespread off-target and dsDNA-nicking effects. *J. Biol. Chem.* **295**, 5538–5553.
- Nishimasu, H., Ran, F.A., Hsu, P.D., Konermann, S., Shehata, S.I., Dohmae, N., Ishitani, R., Zhang, F., and Nureki, O. (2014). Crystal structure of Cas9 in complex with guide RNA and target DNA. *Cell* **156**, 935–949.

- O'Connell, M.R., Oakes, B.L., Sternberg, S.H., East-Seletsky, A., Kaplan, M., and Doudna, J.A. (2014). Programmable RNA recognition and cleavage by CRISPR/Cas9. *Nature* 516, 263–266.
- O'Geen, H., Henry, I.M., Bhakta, M.S., Meckler, J.F., and Segal, D.J. (2015). A genome-wide analysis of Cas9 binding specificity using ChIP-seq and targeted sequence capture. *Nucleic Acids Res.* 43, 3389–3404.
- Okafor, I.C., Singh, D., Wang, Y., Jung, M., Wang, H., Mallon, J., Bailey, S., Lee, J.K., and Ha, T. (2019). Single molecule analysis of effects of non-canonical guide RNAs and specificity-enhancing mutations on Cas9-induced DNA unwinding. *Nucleic Acids Res.* 47, 11880–11888.
- O'Reilly, D., Kartje, Z.J., Ageely, E.A., Malek-Adamian, E., Habibian, M., Schofield, A., Barkau, C.L., Rohilla, K.J., DeRossett, L.B., Weigle, A.T., et al. (2019). Extensive CRISPR RNA modification reveals chemical compatibility and structure-activity relationships for Cas9 biochemical activity. *Nucleic Acids Res.* 47, 546–558.
- Pacesa, M., Loeff, L., Querques, I., Muckenfuss, L.M., Sawicka, M., and Jinek, M. (2022). R-loop formation and conformational activation mechanisms of Cas9. *Nature* 609, 191–196.
- Palermo, G., Chen, J.S., Ricci, C.G., Rivalta, I., Jinek, M., Batista, V.S., Doudna, J.A., and McCammon, J.A. (2018). Key role of the REC lobe during CRISPR-Cas9 activation by “sensing”, “regulating”, and “locking” the catalytic HNH domain. *Q. Rev. Biophys.* 51, e91.
- Pattanayak, V., Lin, S., Gulinger, J.P., Ma, E., Doudna, J.A., and Liu, D.R. (2013). High-throughput profiling of off-target DNA cleavage reveals RNA-programmed Cas9 nuclease specificity. *Nat. Biotechnol.* 31, 839–843.
- Pettersen, E.F., Goddard, T.D., Huang, C.C., Meng, E.C., Couch, G.S., Croll, T.I., Morris, J.H., and Ferrin, T.E. (2021). UCSF ChimeraX: structure visualization for researchers, educators, and developers. *Protein Sci.* 30, 70–82.
- Poornam, G.P., Matsumoto, A., Ishida, H., and Hayward, S. (2009). A method for the analysis of domain movements in large biomolecular complexes. *Proteins* 76, 201–212.
- Ricci, C.G., Chen, J.S., Miao, Y., Jinek, M., Doudna, J.A., McCammon, J.A., and Palermo, G. (2019). Deciphering off-target effects in CRISPR-Cas9 through accelerated molecular dynamics. *ACS Cent. Sci.* 5, 651–662.
- Rodnina, M.V., and Wintermeyer, W. (2001). Fidelity of aminoacyl-tRNA selection on the ribosome: kinetic and structural mechanisms. *Annu. Rev. Biochem.* 70, 415–435.
- Rohs, R., West, S.M., Liu, P., and Honig, B. (2009a). Nuance in the double-helix and its role in protein-DNA recognition. *Curr. Opin. Struct. Biol.* 19, 171–177.
- Rohs, R., West, S.M., Sosinsky, A., Liu, P., Mann, R.S., and Honig, B. (2009b). The role of DNA shape in protein-DNA recognition. *Nature* 461, 1248–1253.
- Salomon-Ferrer, R., Götz, A.W., Poole, D., Le Grand, S., and Walker, R.C. (2013). Routine microsecond molecular dynamics simulations with AMBER on GPUs. 2. Explicit solvent particle mesh Ewald. *J. Chem. Theory Comput.* 9, 3878–3888.
- Semenova, E., Jore, M.M., Datsenko, K.A., Semenova, A., Westra, E.R., Wanner, B., van der Oost, J., Brouns, S.J., and Severinov, K. (2011). Interference by clustered regularly interspaced short palindromic repeat (CRISPR) RNA is governed by a seed sequence. *Proc. Natl. Acad. Sci. USA* 108, 10098–10103.
- Singh, D., Sternberg, S.H., Fei, J., Doudna, J.A., and Ha, T. (2016). Real-time observation of DNA recognition and rejection by the RNA-guided endonuclease Cas9. *Nat. Commun.* 7, 12778.
- Stemmer, M., Thumberger, T., Del Sol Keyer, M., Wittbrodt, J., and Mateo, J.L. (2015). CCTop: an intuitive, flexible and reliable CRISPR/Cas9 target prediction tool. *PLoS One* 10, e0124633.
- Sternberg, S.H., LaFrance, B., Kaplan, M., and Doudna, J.A. (2015). Conformational control of DNA target cleavage by CRISPR-Cas9. *Nature* 527, 110–113.
- Sternberg, S.H., Redding, S., Jinek, M., Greene, E.C., and Doudna, J.A. (2014). DNA interrogation by the CRISPR RNA-guided endonuclease Cas9. *Nature* 507, 62–67.
- Timsit, Y. (1999). DNA structure and polymerase fidelity. *J. Mol. Biol.* 293, 835–853.
- Tsai, S.Q., Nguyen, N.T., Malagon-Lopez, J., Topkar, V.V., Aryee, M.J., and Joung, J.K. (2017). CIRCLE-seq: a highly sensitive in vitro screen for genome-wide CRISPR-Cas9 nuclease off-targets. *Nat. Methods* 14, 607–614.
- Tsai, S.Q., Zheng, Z., Nguyen, N.T., Liebers, M., Topkar, V.V., Thapar, V., Wyvekens, N., Khayter, C., Iafrate, A.J., Le, L.P., et al. (2015). GUIDE-seq enables genome-wide profiling of off-target cleavage by CRISPR-Cas nucleases. *Nat. Biotechnol.* 33, 187–197.
- Turq, P., Lantelme, F., and Friedman, H.L. (1977). Brownian dynamics: its application to ionic solutions. *J. Chem. Phys.* 66, 3039–3044.
- van Houte, S., Ekroth, A.K., Broniewski, J.M., Chabas, H., Ashby, B., Bondy-Denomy, J., Gandon, S., Boots, M., Paterson, S., Buckling, A., and Westra, E.R. (2016). The diversity-generating benefits of a prokaryotic adaptive immune system. *Nature* 532, 385–388.
- Vlot, M., Houkes, J., Lochs, S.J.A., Swarts, D.C., Zheng, P., Kunne, T., Mohanraju, P., Anders, C., Jinek, M., van der Oost, J., et al. (2018). Bacteriophage DNA glucosylation impairs target DNA binding by type I and II but not by type V CRISPR-Cas effector complexes. *Nucleic Acids Res.* 46, 873–885.
- Wang, W., Hellinga, H.W., and Beese, L.S. (2011). Structural evidence for the rare tautomer hypothesis of spontaneous mutagenesis. *Proc. Natl. Acad. Sci. USA* 108, 17644–17648.
- Wu, X., Scott, D.A., Kriz, A.J., Chiu, A.C., Hsu, P.D., Dadon, D.B., Cheng, A.W., Trevino, A.E., Konermann, S., Chen, S., et al. (2014). Genome-wide binding of the CRISPR endonuclease Cas9 in mammalian cells. *Nat. Biotechnol.* 32, 670–676.
- Yakovchuk, P., Protozanova, E., and Frank-Kamenetskii, M.D. (2006). Base-stacking and base-pairing contributions into thermal stability of the DNA double helix. *Nucleic Acids Res.* 34, 564–574.
- Yang, M., Peng, S., Sun, R., Lin, J., Wang, N., and Chen, C. (2018). The conformational dynamics of Cas9 governing DNA cleavage are revealed by single-molecule FRET. *Cell Rep.* 22, 372–382.
- Yaung, S.J., Esvelt, K.M., and Church, G.M. (2014). CRISPR/Cas9-mediated phage resistance is not impeded by the DNA modifications of phage T4. *PLoS One* 9, e98811.
- Yin, H., Song, C.Q., Suresh, S., Kwan, S.Y., Wu, Q., Walsh, S., Ding, J., Bogorad, R.L., Zhu, L.J., Wolfe, S.A., et al. (2018). Partial DNA-guided Cas9 enables genome editing with reduced off-target activity. *Nat. Chem. Biol.* 14, 311–316.
- Yin, H., Song, C.Q., Suresh, S., Wu, Q., Walsh, S., Rhym, L.H., Mintzer, E., Bolukbasi, M.F., Zhu, L.J., Kauffman, K., et al. (2017). Structure-guided chemical modification of guide RNA enables potent non-viral in vivo genome editing. *Nat. Biotechnol.* 35, 1179–1187.
- Zeng, Y., Cui, Y., Zhang, Y., Zhang, Y., Liang, M., Chen, H., Lan, J., Song, G., and Lou, J. (2018). The initiation, propagation and dynamics of CRISPR-SpyCas9 R-loop complex. *Nucleic Acids Res.* 46, 350–361.
- Zgarbová, M., Otyepka, M., Sponer, J., Mládek, A., Banáš, P., Cheatham, T.E., 3rd, and Jurečka, P. (2011). Refinement of the Cornell et al. nucleic acids force field based on reference quantum chemical calculations of glycosidic torsion profiles. *J. Chem. Theory Comput.* 7, 2886–2902.
- Zhang, L., Rube, H.T., Vakulskas, C.A., Behlke, M.A., Bussemaker, H.J., and Pufall, M.A. (2020). Systematic in vitro profiling of off-target affinity, cleavage and efficiency for CRISPR enzymes. *Nucleic Acids Res.* 48, 5037–5053.
- Zhu, X., Clarke, R., Puppala, A.K., Chittori, S., Merk, A., Merrill, B.J., Simonović, M., and Subramaniam, S. (2019). Cryo-EM structures reveal coordinated domain motions that govern DNA cleavage by Cas9. *Nat. Struct. Mol. Biol.* 26, 679–685.

STAR★METHODS

KEY RESOURCES TABLE

REAGENT or RESOURCE	SOURCE	IDENTIFIER
Chemicals, peptides, and recombinant proteins		
Alt-R® S.p. Cas9 Nuclease V3	IDT	Cat# 1081058
RoboSep Filter Tip Racks (8)	StemCell Technologies	Cat# 20125
Lonza Nucleofection Kits (10 96-well plates and buffer) P3	Lonza Walkersville, Inc.	Cat# V4SP-3960
Recombinant Human IL-2	PeproTech, Inc	Cat# 200-02
QuickExtract™ DNA Extraction Solution (10 mL Aliquots)	Lucigen	Cat# QE09050-PQ1329
RoboSep™ Buffer (5X Concentrate)	StemCell Technologies	Cat# 20124
RoboSep Kit # 17951 (Human T cell Isolation Kit)	StemCell Technologies	Cat# 17951
Dynabeads Human T-Activator CD3/CD28 (5 x 2 mL)	Fisher Scientific Co LLC	Cat# 11132D
DNase I Solution (1 mg/mL, 1 mL)	StemCell Technologies	Cat# 7900
Antibiotic/Antmycotic (6 x 100 mL)	Fisher Scientific Co LLC	Cat# MT30004CI
CTS Immune Cell Serum Replacement (50 mL)	ThermoFisher Scientific	Cat# A2596101
Immunocult-XF T Cell Expansion Media	StemCell Technologies	Cat# 10981
SPRIselect Reagent Kit	Beckman Coulter	Cat# B233318
Dynabeads® M-280 Streptavidin	Invitrogen	Cat# 11206D
Q5® Hot Start High-Fidelity 2x Master Mix	New England Biolabs	Cat# M0494L
NEBNext® double-stranded DNA (dsDNA) Fragmentase®	New England Biolabs	Cat# M0348L
T4 DNA Ligase	New England Biolabs	Cat# M0202S
10x T4 DNA Ligase Reaction Buffer	New England Biolabs	Cat# B0202S
Proteinase K	ThermoFisher Scientific	Cat# E00491
HEPES	Roth	Cat# HN78.1
Magnesium chloride	Fluka	Cat# 63064-500G
Potassium chloride	Roth	Cat# 6781.2
Potassium thiocyanate	Roth	Cat# P753.1
Poly(ethylene glycol) 3,350	Sigma-Aldrich	Cat# 202444-500G
Ethylenediaminetetraacetic acid	Roth	Cat# 8040.3
Ni Sepharose 6 Fast Flow resin (500 mL)	Cytiva	CAT# 17-5318-03
HiPrep 26/10 desalting columns (pack of 4)	Cytiva	CAT# 17-5087-02
5 mL HiTrap SP HP	Cytiva	CAT# 17-1152-01
HiLoad Superdex 200 26/600	Cytiva	CAT# 28-9893-36
Critical commercial assays		
NextSeq 500/550 High Output V2.5 (150 cycles)	Illumina	Cat# 20024907
MiSeq Reagent Kit v2 (300- cycles)	Illumina, Inc	Cat# MS-102- 2002
NextSeq PhiX Control Kit	Illumina, Inc	Cat# FC-110- 3002
Blood & Cell Culture DNA Maxi Kit	Qiagen	Cat# 13323
High Sensitivity DNA Bioanalyzer Kit	Agilent	Cat# 5067-4626
NEBNext® dA-tailing Kit	NEB	Cat# E6053L
NEBNext® Ultra End Repair / dA-tailing module	NEB	Cat# E7442L
NEBNext® Ultra Ligation Kit	NEB	Cat# E7445L
NextSeq 500/550 High Output V2.5 (150 cycles)	Illumina	Cat# 20024907
Deposited data		
Atomic coordinates and structure factors of the ternary SpCas9 complex bound to the AAVS1 on-target DNA substrate	Donohoue et al., 2021	PDB: 7OX9
Atomic coordinates and structure factors of the ternary SpCas9 complex bound to the AAVS1 off-target #1 DNA substrate	This study	PDB: 7QQO

(Continued on next page)

Continued

REAGENT or RESOURCE	SOURCE	IDENTIFIER
Atomic coordinates and structure factors of the ternary SpCas9 complex bound to the AAVS1 off-target #2 DNA substrate	This study	PDB: 7QR7
Atomic coordinates and structure factors of the ternary SpCas9 complex bound to the AAVS1 off-target #3 DNA substrate	This study	PDB: 7QQP
Atomic coordinates and structure factors of the ternary SpCas9 complex bound to the AAVS1 off-target #4 DNA substrate	This study	PDB: 7QQQ
Atomic coordinates and structure factors of the ternary SpCas9 complex bound to the AAVS1 off-target #5 DNA substrate	This study	PDB: 7QQR
Atomic coordinates and structure factors of the ternary SpCas9 complex bound to the FANCF on-target DNA substrate	This study	PDB: 7QQS
Atomic coordinates and structure factors of the ternary SpCas9 complex bound to the FANCF off-target #1 DNA substrate	This study	PDB: 7QQT
Atomic coordinates and structure factors of the ternary SpCas9 complex bound to the FANCF off-target #2 DNA substrate	This study	PDB: 7QQU
Atomic coordinates and structure factors of the ternary SpCas9 complex bound to the FANCF off-target #3 DNA substrate	This study	PDB: 7QQV
Atomic coordinates and structure factors of the ternary SpCas9 complex bound to the FANCF off-target #4 DNA substrate	This study	PDB: 7QQW
Atomic coordinates and structure factors of the ternary SpCas9 complex bound to the FANCF off-target #5 DNA substrate	This study	PDB: 7QQX
Atomic coordinates and structure factors of the ternary SpCas9 complex bound to the FANCF off-target #6 DNA substrate	This study	PDB: 7QR5
Atomic coordinates and structure factors of the ternary SpCas9 complex bound to the FANCF off-target #7 DNA substrate	This study	PDB: 7QQZ
Atomic coordinates and structure factors of the ternary SpCas9 complex bound to the PTPRC off-target #1 DNA substrate	This study	PDB: 7QR8
Atomic coordinates and structure factors of the ternary SpCas9 complex bound to the TRAC on-target DNA substrate	Donohoue et al., 2021	PDB: 7OX8
Atomic coordinates and structure factors of the ternary SpCas9 complex bound to the TRAC off-target #1 DNA substrate	This study	PDB: 7QR0
Atomic coordinates and structure factors of the ternary SpCas9 complex bound to the TRAC off-target #2 DNA substrate	This study	PDB: 7QR1
Atomic coordinates and structure factors of the ternary SpCas9 complex bound to the CD34 off-target #9 DNA substrate	This study	PDB: 7ZO1
Raw SITE-Seq data	This study	BioProject ID: PRJNA862989
Raw SITE-Seq data – TRAC target	Donohoue et al., 2021	BioProject ID: PRJNA744493
Bacterial and virus strains		
E. coli Rosetta 2 (DE3)	Novagen	Cat# 71400-3
Oligonucleotides		
Transcription templates, cleavage substrates, crystallization substrates	This study	Table S9
Recombinant DNA		
pMJ806 (WT SpCas9)	AddGene	#39312
pMJ841 (SpCas9 D10A, H840A)	AddGene	#39318
Software and algorithms		
XDS	Kabsch, 2010	http://xds.mpimf-heidelberg.mpg.de/
Phenix	Adams et al., 2010	http://www.phenix-online.org/
PyMOL	The PyMOL Molecular Graphics System, Version 2.0 Schrödinger, LLC	https://www.pymol.org/
DynDom	Poornam et al., 2009	http://fizz.cmp.uea.ac.uk/dyndom/

(Continued on next page)

Continued

REAGENT or RESOURCE	SOURCE	IDENTIFIER
PDBePISA	Krissinel and Henrick, 2007	http://www.ebi.ac.uk/pdbe/pisa/
ChimeraX	Pettersen et al., 2021	https://www.rbvi.ucsf.edu/chimerax/
GraphPad Prism 9	GraphPad Prism 9 for Windows, Version 9.1.2.	https://www.graphpad.com
MolProbity	Chen et al., 2010	http://molprobity.biochem.duke.edu
COOT	Emsley et al., 2010	https://www2.mrc-lmb.cam.ac.uk/personal/pemsley/coot/

RESOURCE AVAILABILITY

Lead contact

Further information and requests for resources and reagents should be directed to and will be fulfilled by the lead contact, Prof. Martin Jinek (jinek@bioc.uzh.ch)

Materials availability

This study did not generate new unique reagents.

Data and code availability

- Coordinates have been deposited to the Protein Data Bank under PDB: 7QOQ, 7QR7, 7QQP, 7QQQ, 7QQR, 7QQS, 7QQT, 7QQU, 7QQV, 7QQW, 7QQX, 7QR5, 7QQZ, 7QR8, 7QR0, 7QR1, 7ZO1 accession codes. Raw sequencing files for the SITE-Seq assay have been deposited to BioProject. Accession numbers are listed in the [key resources table](#). All deposited data is publicly available as of the date of publication.
- This paper does not report original code.
- Any additional information required to reanalyze the data reported in this paper is available from the lead contact upon request.

EXPERIMENTAL MODEL AND SUBJECT DETAILS

The *E. coli* strains Rosetta 2 (DE3) was used for recombinant protein expression for structural studies and biochemical *in vitro* experiments. T cells used for cellular editing experiments were isolated from human primary blood mononuclear cells were purchased from STEMCELL Technologies.

METHOD DETAILS

DNA oligonucleotides and substrates

Sequences of DNA oligonucleotides used in this study are summarized in [Data S1](#). Crystallization substrates were synthesized by Sigma Aldrich without further purification, sgRNA transcription templates and ATTO-532-labelled cleavage substrates were synthesized by Integrated DNA Technologies, Inc., with PAGE and HPLC purification, respectively. Partially double-stranded crystallization substrates were prepared by mixing complementary oligonucleotides in a 1:1 molar ratio (as determined by 260 nm absorption), heating to 95 °C for 5 minutes and slow cooling to room-temperature. Cleavage substrates were prepared similarly, except that a 2-fold molar excess of the non-target strand was used.

Cas9 protein expression and purification

Streptococcus pyogenes Cas9 wild-type and the nuclease-dead mutant (D10A, H840A) proteins were recombinantly expressed for 16 hours at 18 °C in *Escherichia coli* Rosetta 2 (DE3) (Novagen) N-terminally fused to a hexahistidine affinity tag, the maltose binding protein (MBP) polypeptide, and the tobacco etch virus (TEV) protease cleavage site. Cells were resuspended and lysed in 20 mM HEPES-KOH pH 7.5, 500 mM KCl, 5 mM imidazole, and supplemented with added protease inhibitors. Clarified lysate was loaded on a 10 ml Ni-NTA Superflow column (QIAGEN), washed with 7 column volumes of 20 mM HEPES-KOH pH 7.5, 500 mM KCl, 5 mM imidazole, and eluted with 10 column volumes of 20 mM HEPES-KOH pH 7.5, 250 mM KCl, 200 mM imidazole. Salt concentration was adjusted and protein was loaded on a 10 ml HiTrap Heparin HP column (GE Healthcare) equilibrated in 20 mM HEPES-KOH pH 7.5, 250 mM KCl, 1 mM DTT. The column was washed with 5 column volumes of 20 mM HEPES-KOH pH 7.5, 250 mM KCl, 1 mM DTT, and Cas9 was eluted with 17 column volumes of 20 mM HEPES-KOH pH 7.5, 1.5 M KCl, 1 mM DTT, in a 0-32% gradient (peak elution around 500 mM KCl). His₆-MBP tag was removed by TEV protease cleavage overnight. The untagged Cas9 was concentrated and applied to a Superdex 200 16/600 (GE Healthcare) and eluted with 20 mM HEPES-KOH pH 7.5, 500 mM KCl, 1 mM DTT. Purified

protein was concentrated to 10 mg/ml, flash frozen in liquid nitrogen and store at -80°C . DTT was omitted in the size-exclusion step of the purification when protein was used for switchSENSE measurements.

sgRNA transcription and purification

sgRNAs were transcribed from a double stranded PCR product template amplified from a plasmid in a 5 ml transcription reaction (30 mM Tris-HCl pH 8.1, 25 mM MgCl_2 , 2 mM spermidine, 0.01% Triton X-100, 5 mM CTP, 5 mM ATP, 5 mM GTP, 5 mM UTP, 10 mM DTT, 1 μM DNA transcription template, 0.5 units inorganic pyrophosphatase (Thermo Fischer), 250 μg homemade T7 RNA polymerase. The reaction was incubated at 37°C for 5 hours, and then treated for 30 minutes with 15 units of RQ1 DNase (Promega). The transcribed sgRNAs were subsequently PAGE purified on an 8% denaturing (7 M urea) polyacrylamide gel, and lastly ethanol precipitated and resuspended in DEPC treated water.

Crystallization of Cas9 ternary complexes and structure determination

To assemble the Cas9 on-/off-target ternary complexes, the Cas9 protein was first mixed with the sgRNA in a 1:1.5 molar ratio and incubated at room temperature for 10 minutes. Next, the binary complex was diluted to 2 mg/ml with 20 mM HEPES-KOH 7.5, 250 mM KCl, 1 mM DTT, 2 mM MgCl_2 buffer, pre-annealed 100 μM DNA substrate is added in a 1:1.8 molar ratio and the complex was incubated for another 10 minutes at room temperature. For crystallization, 1 μl of the ternary complex (1–2 mg/ml) was mixed with 1 μl of the reservoir solution (0.1 M Tris-acetate pH 8.5, 0.3–0.5 M KSCN, 17–19% PEG3350) and crystals were grown at 20°C using the hanging drop vapour diffusion method. In some cases, microseeding was used to improve crystal morphology. Crystals were harvested after 2–3 weeks, cryoprotected in 0.1 M Tris-acetate pH 8.5, 0.4 M KSCN, 30% PEG3350, 15% ethylene glycol, 1 mM MgCl_2 , and flash-cooled in liquid nitrogen. Diffraction data was measured at beamlines PXI and PXIII of the Swiss Light Source (Paul Scherrer Institute, Villigen, Switzerland) and processed using the XDS package (Kabsch, 2010). Structures were solved by molecular replacement through the Phaser module of the Phenix package (Adams et al., 2010) using the PDB ID: 5FQ5 model omitting the RNA-DNA target duplex from the search. Model adjustment and duplex building was completed using COOT software (Emsley et al., 2010). Atomic model refinement was performed using Phenix.refine (Adams et al., 2010). Model validation was performed using MolProbity (Chen et al., 2010). Protein-nucleic acid interactions were analyzed using the PISA web server (Krissinel and Henrick, 2007). Conformational geometry analysis of the guide-protospacer duplex was performed using the 3DNA 2.0 web server (Li et al., 2019). Structural figures were generated using PyMOL and ChimeraX (Pettersen et al., 2021). Domain movement was analyzed using DynDom (Poornam et al., 2009).

In vitro nuclease activity assays

Cleavage reactions were performed at 37°C in reaction buffer, containing 20 mM HEPES pH 7.5, 250 mM KCl, 5 mM MgCl_2 and 1 mM DTT. First, Cas9 protein was pre-incubated with sgRNA in 1:1.25 ratio for 10 minutes at room temperature. The protein-sgRNA complex was rapidly mixed with the target strand-ATTO-532-labelled dsDNA, to yield final concentrations of 1.67 μM protein-sgRNA complex and 66.67 nM substrate. 7.5 μl aliquots were taken at 1, 2.5, 5, 15, 45, 90, 150 min, and 24 h time points. Cleavage was stopped by addition of 2 μl of 250 mM EDTA, 0.5% SDS and 20 μg of Proteinase K. Formamide was added to the reactions to final concentration of 50%, samples were incubated at 95°C for 10 min, and resolved on a 15% denaturing PAGE gel containing 7 M urea and imaged using a Typhoon FLA 9500 gel imager. Depicted error bars correspond to the standard deviation from four independent cleavage reactions. Rate constants (k_{obs}) were extracted from single exponential fits: $[\text{Product}] = A^*(1 - \exp(-k_{\text{obs}} * t))$

switchSENSE analysis

Target strand (TS) oligonucleotides containing a 3' flanking sequence complementary to the ssDNA covalently bound to the chip electrode, and the non-target strands (NTS) (Data S1) were dissolved in a buffer containing 10 mM Tris-HCl pH 7.4, 40 mM NaCl, and 0.05% Tween 20. The TS:NTS duplexes were pre-annealed and hybridized to the chip anode. Cas9 protein was mixed with sgRNAs at a 1:2 (protein:RNA) molar ratio, and the complex was incubated for 30 min at 37°C in association buffer containing 20 mM HEPES-KOH pH 7.5, 150 mM KCl, 2 mM MgCl_2 , 0.01% Tween 20. All switchSENSE experiments were performed on a DRX analyzer using CAS-48-1-R1-S chips (Dynamic Biosensors GmbH, Martinsried, Germany). Kinetics experiments were performed at 25°C in association buffer, with an association time of 5 min, dissociation time of 20 min, and a flow rate of 50 $\mu\text{l}/\text{min}$.

SITE-Seq assay

SITE-Seq assay reaction conditions were performed as described previously (Cameron et al., 2017). Briefly, high molecular weight genomic DNA (gDNA) was purified from human primary T cells using the Blood & Cell Culture DNA Maxi Kit (Qiagen) according to the manufacturer's instructions. Cas9 RNPs were assembled as follows. Equal molar amounts of crRNA and tracrRNA were mixed and heated to 95°C for 2 min then allowed to cool at room temperature for ~ 5 min. Three-fold molar excess of the crRNA-tracrRNA guide was incubated with SpCas9 in cleavage reaction buffer (20 mM HEPES pH 7.4, 150 mM KCl, 10 mM MgCl_2 , 5% glycerol) at 37°C for 10 min. In a 96-well plate format, 10 μg of gDNA was treated with 0.2 pmol (4 nM), 0.8 pmol (16 nM), 3.2 pmol (64 nM), and 12.8 pmol (256 nM) of each RNP in 50 μl total volume in cleavage reaction buffer. Each cleavage reaction was performed in triplicate. Negative control reactions lacking Cas9-gRNA RNP were assembled in parallel. gDNA was treated with RNPs for 4 hours at 37°C . SITE-Seq

assay library preparation and sequencing was performed as described previously and the final library was loaded onto the Illumina NextSeq platform (Illumina, San Diego, CA). ~1-3 million reads were obtained for each sample.

SITE-Seq assay analysis and selection for cellular validation

SITE-Seq assay recovered off-targets were filtered for sites that had read-pileups proximal to the expected cut site, a PAM comprising at least one guanine base, fewer than 12 mismatches (reasoning that sites with 12 or more mismatches are likely spurious peaks not resulting from Cas9-induced double-strand breaks), and all sites with 11 mismatches were visually inspected and included in analysis if a putative deletion or insertion would result in a reduction of at least 4 mismatches relative to the spacer sequence.

***In silico* mismatch, deletion, and insertion classification**

Predictive classification of SITE-Seq assay recovered off-target sites as pure mismatches, deletions, or insertions was executed using a scoring algorithm which consisted of the following sequential steps: (i) For each off-target, a gap library was generated where a single nucleotide gap was introduced between each nucleotide in the off-target sequence. (ii) The off-target gap library was then aligned to the spacer sequence and each alignment was scored based on the number of matched bases between the spacer and gapped off-target pair. If the gapped off-target with the highest alignment score improved alignment by at least 4 nucleotides relative to the non-gapped spacer-off-target alignment, the off-target sequence was marked as a single-nucleotide deletion and removed from subsequent analysis. (iii) The remaining pool of off-targets were then aligned to a spacer gapped library where a single nucleotide gap was introduced at each positing in the spacer. (iv) The spacer gap library was then aligned to each off-target sequence and each alignment was scored based on the number of matched bases between the off-target and the gapped spacer pair. If the gapped spacer with the highest alignment score improved alignment by at least 4 nucleotides relative to the non-gapped spacer-off-target alignment, the off-target sequence was marked as a single-nucleotide insertion and removed from subsequent analysis. (v) The remaining off-targets for which the spacer-off-target alignment was not improved by single-nucleotide deletions or insertions were annotated as a mismatched off-targets.

Generation of ribonucleoprotein complexes (RNP) for electroporation

Synthetic crRNA and tracrRNA oligonucleotides were ordered from Integrated DNA Technologies (Coralville, IA) as AltR™ reagents. Ribonucleoprotein complexes (RNPs) were formulated by incubating 480 pmol of each crRNA and tracrRNA and heated to 95 °C for 2 min, then allowed to cool at room temperature for ~5 min. Annealed guides were mixed with 160 pmol of Cas9 protein (1:3 molar ratio of Cas9 to guide RNA) in RNP assembly buffer (20 mM HEPES pH 7.4, 150 mM KCl, 10 mM MgCl₂, 5% glycerol) and incubated at 37 °C for 10 min. RNPs were then serially diluted two-fold by mixing with equal volume of RNP assembly buffer across seven concentrations down to 2.5 pmol of Cas9 and 7.5 pmol of crRNA-tracrRNA. RNPs were kept at 4 °C or on ice until electroporation.

T cell handling and nucleofection

T cells were isolated from peripheral blood mononuclear cells (PBMCs) using the RoboSep-S cell isolation platform (STEMCELL Technologies) with EasySep Human T cell Isolation Kit (STEMCELL Technologies). Cells were then activated for 3 days in “Complete media” (Immuncult-XF T cell expansion media (STEMCELL Technologies), CTS Immune Cell serum replacement (Fisher Scientific), 1x antibiotic-antimycotic (Fisher Scientific), and recombinant human Interleukin-2 (rhIL-2, 100 units/ml)) in the presence of anti-CD3/CD28 Dynabeads (Fisher Scientific) at a bead:cell ratio of 1:1. On the third day, beads were removed and cells expanded in Complete media for 24 hours. Cells were then harvested, washed once with phosphate-buffered saline (PBS) and resuspended at 10⁷ cells/ml in P4 Primary Cell Nucleofector Solution (Lonza). 20 μL of resuspended cells (corresponding to ~200,000 cells) were then combined with 2.5 μL of RNP and electroporated using the Lonza 4D 96-well Nucleofector electroporation system using pulse code CA137. Transfected cells were then recovered in 180 μL/sample of Complete media. After 48 hours, the electroporated T cells were pelleted and gDNA was isolated by adding 50 μL/well QuickExtract DNA extraction solution (Epicentre), followed by incubation at 37 °C for 10 minutes, 65 °C for 6 minutes, and 95 °C for 3 minutes. The isolated gDNA was diluted with 50 μL sterile water to achieve ~2,000 genome equivalents/μL and samples were stored at -20 °C until sequencing analysis.

Targeted amplicon sequencing

On- and off-target sites were amplified in a two-step PCR reaction. In brief, 3.75 μL (corresponding to ~7,500 cells) of lysate was used as a template for PCR amplification with Q5 Hot-Start High Fidelity DNA Polymerase (NEB) and unique primer pairs containing an internal locus-specific region and an outer Illumina-compatible adapter sequence. A second PCR reaction targeting the outer-adapter sequence was performed to append unique indices to each amplicon. Sites were sequenced on a MiSeq with 2 × 151 paired-end reads and v2 chemistry, or NextSeq with 2 × 151 paired-end reads and v2 or v2.5 chemistry (Illumina), and aligned to the hg38 genomic assembly. For each site, indels were tallied if they occurred within 3 nucleotides of the putative Cas9 cut site, and editing efficiencies were calculated by subtracting the percentage of indels in untransfected cells from the percentage of indels in RNP-transfected cells. Depth of coverage was ~5,000–20,000 reads per amplicon, and all samples with <500 reads aligning to the predicted amplicon were discarded. Lower limit of detection (0.1%) was determined by titration of NIST genomic standards and assessment of expected versus measured values (data not shown).

Molecular Dynamics (MD) simulations

MD simulations were performed using a well-established protocol, previously employed in several computational studies of CRISPR-Cas9 (Mitchell et al., 2020; Ricci et al., 2019). The Amber ff14SB force field (Maier et al., 2015) was adopted, including the ff99bsc1 corrections for DNA (Ivani et al., 2016) and the ff99bsc0+ γ OL3 corrections for RNA (Banáš et al., 2010; Zgarbová et al., 2011). Explicit water molecules were described using the TIP3P model (Jorgensen et al., 1983), while the Li & Merz model was used for Mg^{2+} ions (Li and Merz, 2014). An integration time step of 2 fs was applied. All bond lengths involving hydrogen atoms were constrained using the SHAKE algorithm. Temperature control (300 K) was performed via Langevin dynamics (Turq et al., 1977), with a collision frequency $\gamma = 1$. Pressure control was accomplished by coupling the system to a Berendsen barostat (Berendsen et al., 1984), at a reference pressure of 1 atm and with a relaxation time of 2 ps. The systems were subjected to energy minimization to relax water molecules and counter ions, keeping the protein, the RNA, DNA and Mg^{2+} ions fixed with harmonic position restraints of $300 \text{ kcal/mol} \cdot \text{Å}^2$. Then, the systems were heated up from 0 to 100 K in the canonical ensemble (NVT), by running two simulations of 5 ps each, imposing position restraints of $100 \text{ kcal/mol} \cdot \text{Å}^2$ on the above-mentioned elements of the system. The temperature was further increased up to 200 K in ~ 100 ps of MD in the isothermal-isobaric ensemble (NPT), reducing the restraint to $25 \text{ kcal/mol} \cdot \text{Å}^2$. Subsequently, all restraints were released, and the temperature of the systems was raised up to 300 K in a single NPT simulation of 500 ps. After ~ 1.1 ns of equilibration, ~ 10 ns of NPT runs were carried out allowing the density of the systems to stabilize around 1.01 g cm^{-3} . Finally, production runs were carried out in the NVT ensemble, collecting ~ 500 ns in three replicates for each of the systems. These simulations have been performed using the GPU-empowered version of AMBER 20 (Case, 2021; Salomon-Ferrer et al., 2013). Analysis of the RNA:DNA conformational dynamics has been done using the CURVES+ code (Lavery et al., 2009). Molecular simulations were based on three X-ray structures of CRISPR-Cas9: *TRAC* on-target (PDB: 7OX8), *AAVS1* on-target #2 and *FANCF* on-target, displaying 20 base pair long RNA:TS DNA hybrid and a cleaved NTS. To study the accommodation of rA-dA mismatches at various positions along the heteroduplex, we systematically mutated the base pairs to rA-dA mismatches (*TRAC* on-target for positions 1, 11, 15, and 20; *FANCF* on-target for positions 3-5, 9, and 18; *AAVS1* on-target for positions 2, 6-8, 10, 12-14, 16, 17, and 19), using the LEaP tool in the AMBER 20 code (Lavery et al., 2009). Additionally, the pre-cleavage state crystal structure of CRISPR-Cas9 with no mismatches (PDB: 4UN3) was also simulated for comparison. The obtained model systems were embedded in explicit waters, and counterions were added to neutralize the total charge at physiological conditions, leading to periodic simulation cells of $\sim 145 \times 115 \times 150 \text{ Å}^3$ and a total of $\sim 220,000$ atoms for each system.

QUANTIFICATION AND STATISTICAL ANALYSIS

Error bars, sample size, and data fitting for *in vitro* biochemical cleavage experiments and switchSENSE nanolever assay are indicated in the corresponding figure legends and STAR Methods section. Statistical analysis was performed using GraphPad Prism version 9.1.2. for Windows (GraphPad Software). SITE-seq assay data analysis was performed using a custom built pipeline described in the STAR Methods section.

Supplemental figures

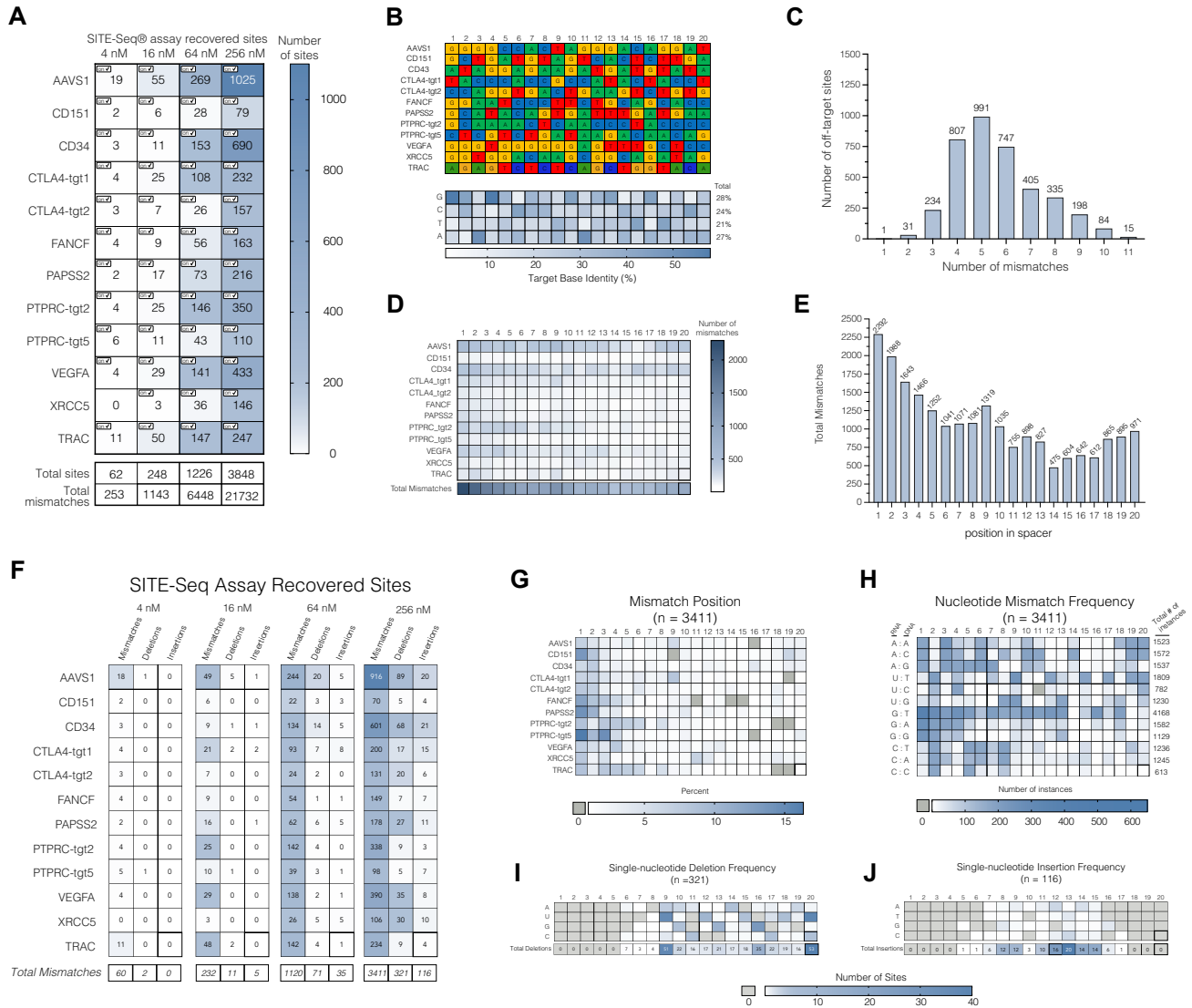
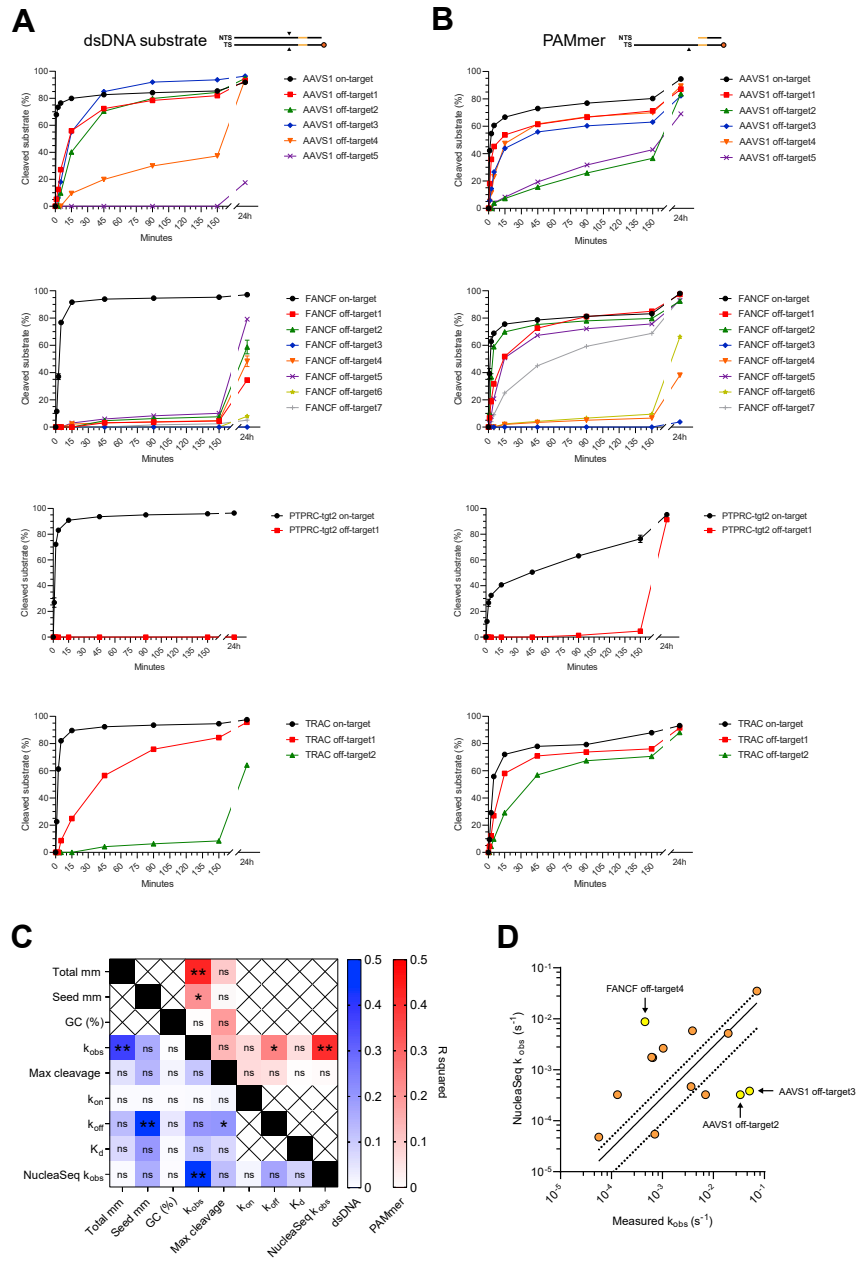


Figure S1. Off-target profiling of selected genomic sites using SITE-Seq, related to Figures 1 and 5

- (A) SITE-Seq assay analysis for selected genomic targets investigated in this study. The numbers of detected off-target sites are shown as a function of Cas9 RNP concentration. Checked boxes indicate recovery of the on-target site. $n = 3$ replicates per sample.
- (B) Genomic targets and the corresponding guide RNA sequences selected for the SITE-Seq assay off-target profiling. Heatmap indicates frequency of nucleotide identity across each position for the selected targets.
- (C) Number of off-target sites recovered by the SITE-Seq assay is shown as a function of the number of mismatches between the guide RNA and the off-target sequence.
- (D) Frequency of nucleotide mismatches at each guide RNA-off-target DNA heteroduplex position for all off-target sites identified in (B).
- (E) Number of total identified mismatches per heteroduplex position.
- (F) Number of recovered off-target sites per genomic target as a function of RNP concentration, classified as containing either only mismatches, single-nucleotide deletions, or single-nucleotide insertions.
- (G) Frequency of positional mismatch occurrence per genomic target for mismatched off-targets.
- (H) Frequency of nucleotide mismatches within the heteroduplex for all off-target sites ($n = 3,411$ sites for both B and C).
- (I) Frequency of single-nucleotide deletions for all off-target sites ($n = 321$ sites).
- (J) Frequency of single-nucleotide insertions for all off-target sites ($n = 116$ sites).

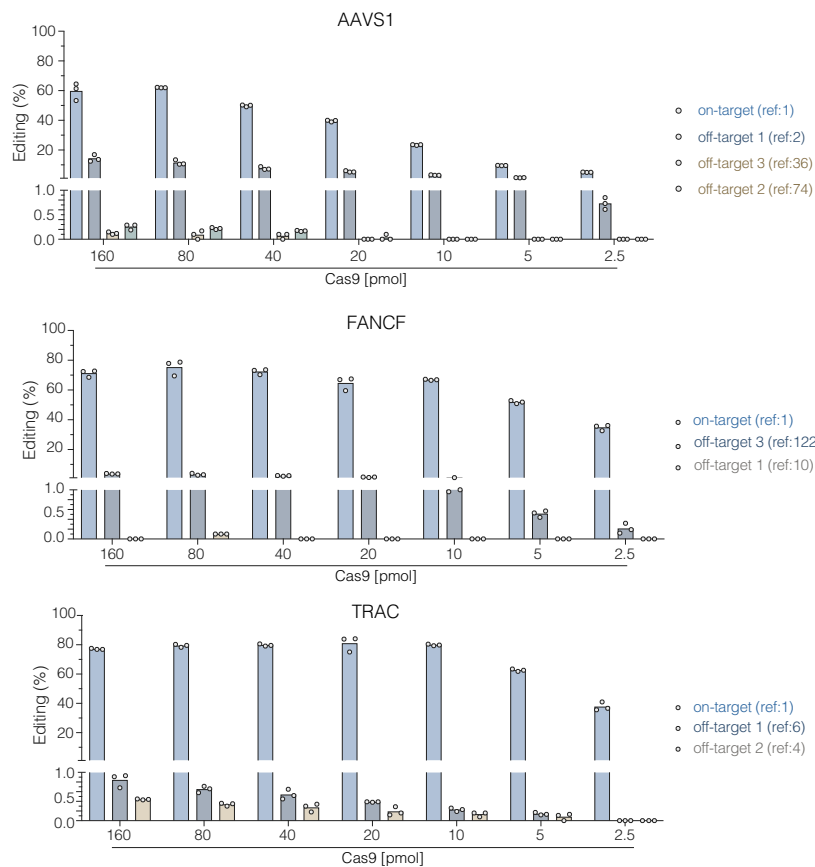


(figure continued on next page)

E

Gene	Sequence	1	2	3	4	5	6	7	8	9	10	11	12	13	14	15	16	17	18	19	20	Editing (%)
AAVS1	guide RNA	G	G	G	G	C	C	A	C	T	A	G	G	G	A	C	A	G	G	A	T	59.7
AAVS1	on-target	C	C	C	C	G	G	T	G	A	T	C	C	C	T	G	T	C	C	T	A	
AAVS1	off-target 1	.	.	.	T	.	.	.	A	G	14.3
AAVS1	off-target 2	A	.	.	.	G	.	G	T	G	A	.	0.3
AAVS1	off-target 3	C	C	0.1
AAVS1	off-target 4	A	A	T	.	<0.1
AAVS1	off-target 5	.	.	T	C	G	G	.	<0.1
FANCF	guide RNA	G	G	A	A	T	C	C	C	T	T	C	T	G	C	A	G	C	A	C	C	71.2
FANCF	on-target	C	C	T	T	A	G	G	G	A	A	G	A	C	G	T	C	G	T	G	G	
FANCF	off-target 1	.	.	.	G	.	.	.	C	<0.1
FANCF	off-target 2	.	.	C	G	.	.	T	<0.1
FANCF	off-target 3	.	.	.	G	3.7
FANCF	off-target 4	T	G	G	G	<0.1
FANCF	off-target 5	A	T	.	.	.	G	<0.1
FANCF	off-target 6	.	.	.	G	T	A	.	T	A	.	.	<0.1
FANCF	off-target 7	A	.	T	<0.1
PTPRC -tgt2	guide RNA	C	G	T	T	T	G	A	G	T	T	G	G	G	A	T	G	G	G	G	84.0	
PTPRC -tgt2	on-target	G	C	A	A	A	C	T	C	A	A	C	C	C	T	A	C	C	C	C		
PTPRC -tgt2	off-target 1	.	.	.	A	.	.	T	0.0	
TRAC	guide RNA	A	G	A	G	T	C	T	C	T	C	A	G	C	T	G	G	T	A	C	A	77.1
TRAC	on-target	T	C	T	C	A	G	A	G	A	G	T	C	G	A	C	C	A	T	G	T	
TRAC	off-target 1	C	T	G	T	0.8	
TRAC	off-target 2	.	T	T	0.4	

F



(legend continued on next page)

Figure S2. *In vitro* and *in vivo* cleavage of selected Cas9 off-target substrates, related to Tables 1 and S2

(A) *In vitro* cleavage kinetics of fully double-stranded on- and off-target synthetic DNA substrates (fluorophore-labeled on the target strand) for each guide RNA used in the study. Black triangles in the substrate schematic (top) indicate position of cleavage sites. Each data point represents a mean of four independent replicates. Error bars represent standard error of the mean for each time point.

(B) *In vitro* cleavage kinetics of partially single-stranded (PAMmer) on- and off-target substrates.

(C) Heatmap representation of mutual correlations between measured kinetic and thermodynamic parameters including cleavage (k_{obs}), substrate DNA binding (k_{on}), substrate dissociation (k_{off}) rate constants, equilibrium dissociation constant (K_{d}) with numbers of nucleotide mismatches in the off-target sites (total and within seed), the guanine-cytosine (GC) content of the spacer (GC %), and cleavage rate predicted using the NucleaSeq algorithm (NucleaSeq k_{obs}). The values represent Pearson correlation with two-tailed p value and were calculated across all off-targets for both dsDNA (lower left half, in blue), and partially single-stranded (PAMmer) substrates (upper right half, in red). ns, no significant correlation. p values: >0.05 (ns), <0.05 (*), <0.01 (**).

(D) Correlation between measured and NucleaSeq-predicted k_{obs} rate constants. Off-target sites with significant deviations are highlighted in yellow.

(E) Editing activity, expressed as frequency of indel mutations, at on- and off-target sites in primary human T cells. Matching bases in off-target sites are denoted by a dot, whereas base pair mismatches and deletions (–) are highlighted. Asterisk indicates single-nucleotide polymorphism in peripheral blood mononuclear cell (PBMC) donor sequence relative to the hg38 genomic reference. Editing rates are from highest Cas9 RNP concentration shown in (F), n = 3 replicates per sample, with a 0.1% limit of detection.

(F) Dose titration of Cas9 RNPs in human primary T cells for selected on- and off-target sites. Off-target numbering corresponds to sample shown in (E) and/or reference number (“ref”), as indicated in Table S1. Cas9 RNP concentrations are shown below x axis, n = 3 replicates per sample.

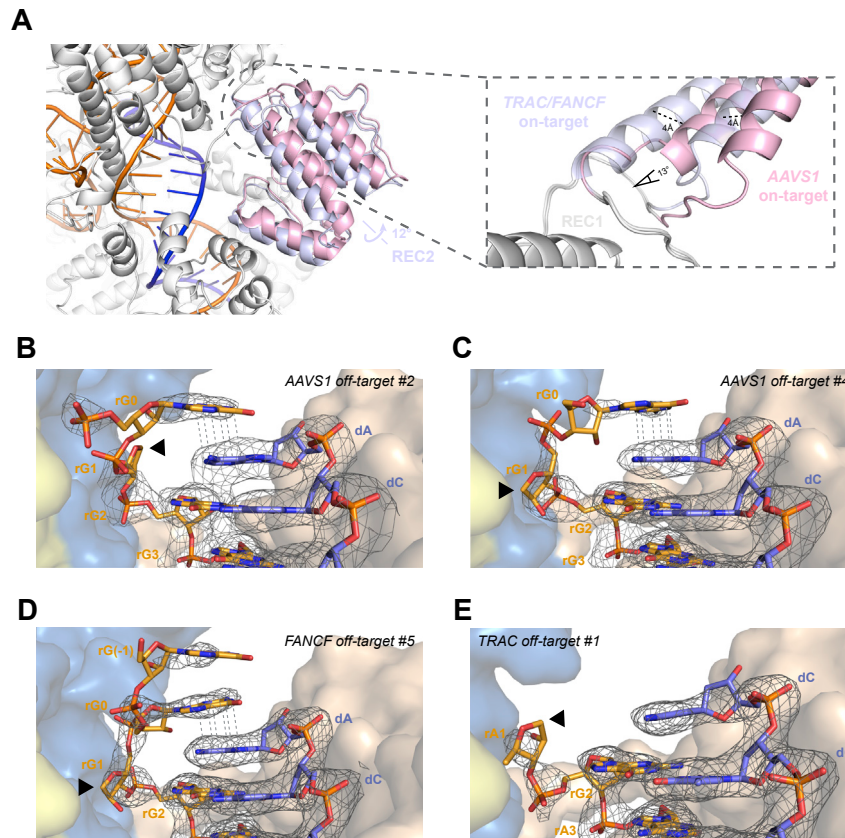


(figure continued on next page)

F

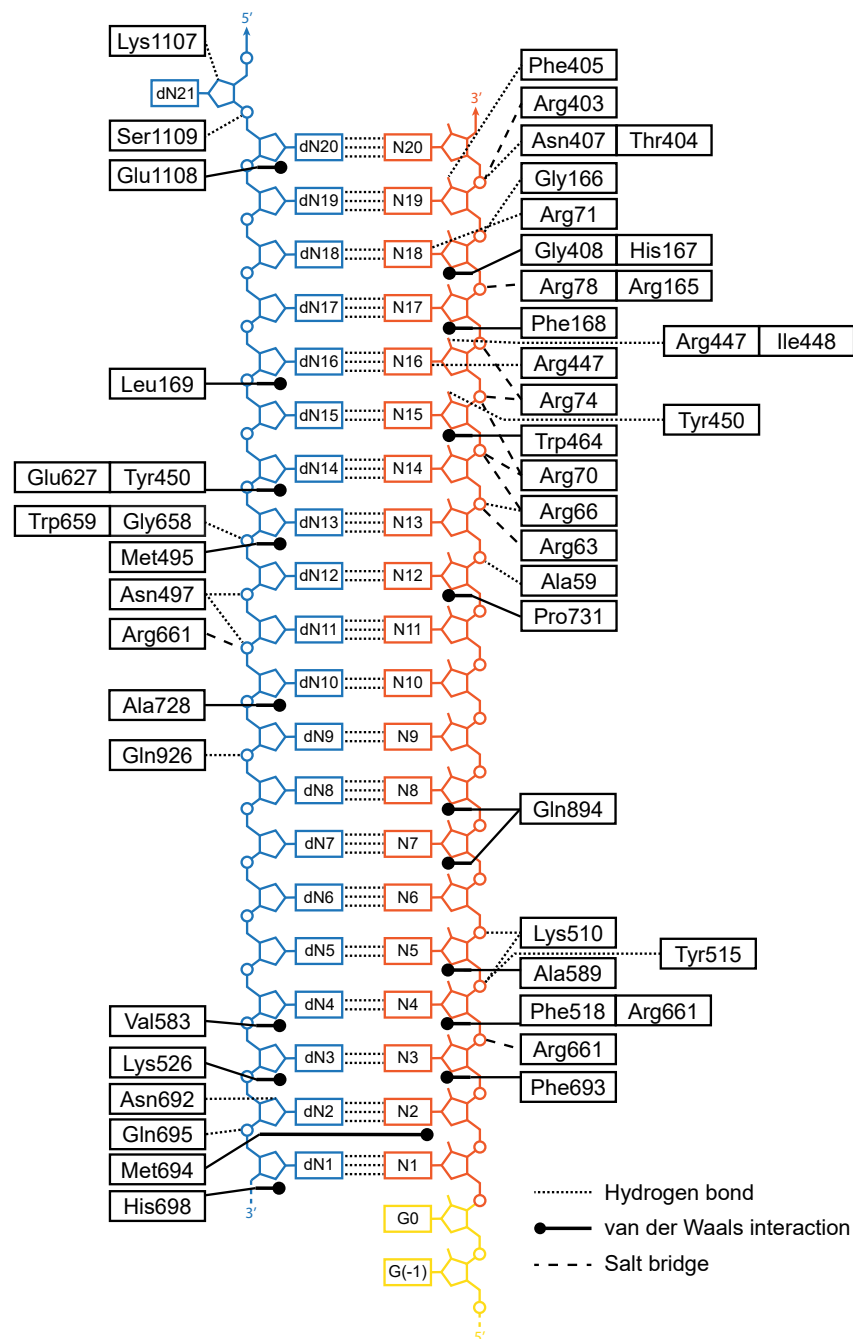
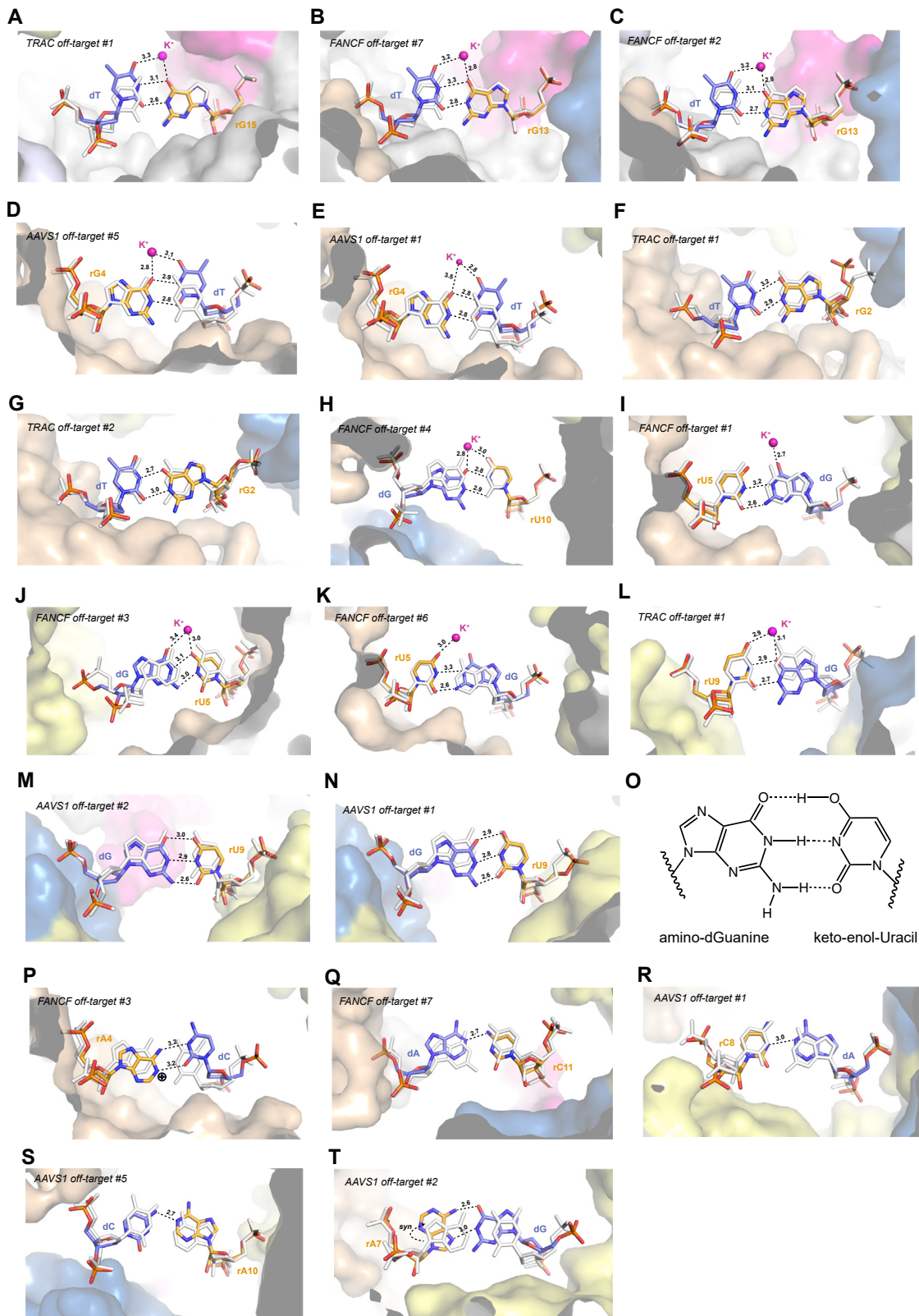


Figure S3. Conformational plasticity and heteroduplex binding in Cas9 off-target complexes, related to Figure 1

(A) Overlay of REC2 domain conformations in the *AAVS1* (pink) and *FANCF/TRAC* (light blue) on-target complexes. Inset shows linear and angular displacements of the domain in the *AAVS1* on-target complex relative to the *FANCF* and *TRAC* on-target complexes.

(B–E) Close-up views of the PAM-distal end of the guide RNA-TS heteroduplex in (B) *AAVS1* off-target #2, (C) *AAVS1* off-target #4, (D) *FANCF* off-target #5, and (E) *TRAC* off-target #1 complexes. Arrowheads indicate nucleotides with structurally disordered bases. Refined $2mF_o - mF_c$ electron density maps of the heteroduplexes are rendered as a gray mesh and contoured at 1.2σ for (B) and 1.0σ for (C)–(E).

(F) Schematic depicting Cas9 residues interacting with the guide RNA-target DNA heteroduplex. Dotted lines represent hydrogen-bonding interactions; dashed lines represent salt bridges; solid lines represent stacking/hydrophobic interactions. Target strand is colored in blue, guide RNA in orange. Phosphates are represented by circles, ribose moieties by pentagons, and nucleobases by rectangles.



(legend on next page)

Figure S4. Position-specific conformations of purine-pyrimidine and purine-purine mismatches, related to Figure 2

(A–G) Close-up views of rG–dT mismatches at (A) heteroduplex position 15 in the *TRAC* off-target #1 complex, (B) position 13 in *FANCF* off-target #7 complex, (C) position 13 in *FANCF* off-target #2 complex, (D) position 4 in *AAVS1* off-target #5 complex, (E) position 4 in *AAVS1* off-target #1 complex, (F) position 2 in *TRAC* off-target #1 complex, and (G) position 2 in *TRAC* off-target #2 complex.

(H–N) Close-up views of rU–dG mismatches at (H) heteroduplex position 10 in *FANCF* off-target #4 complex, (I) position 5 in *FANCF* off-target #1 complex, (J) position 5 in *FANCF* off-target #3 complex, (K) position 5 in *FANCF* off-target #6 complex, (L) position 9 in *TRAC* off-target #1 complex, and (M) position 9 in *AAVS1* off-target #2 complex, and (N) position 9 in *AAVS1* off-target #1 complex.

(O) Schematic representation of the alternative tautomeric forms implied in the n rU–dG base pairs observed in (M) and (N).

(P) Close-up view of rA–dC wobble base pairing at position 4 in *FANCF* off-target #3 complex.

(Q) Close-up view of rC–dA mismatch at position 11 of *FANCF* off-target #7 complex.

(R) Close-up view of partially paired rC–dA mismatch at position 8 in *AAVS1* off-target #1 complex.

(S) Close-up view of rA–dC mismatch at position 10 in *AAVS1* off-target #5 complex.

(T) Close-up view of Hoogsteen-edge rA–dG base pair at position 7 in *AAVS1* off-target #2 complex. Corresponding on-target base pairs are shown superposed and colored white. Monovalent ions, modeled as K^+ , are depicted as purple spheres.

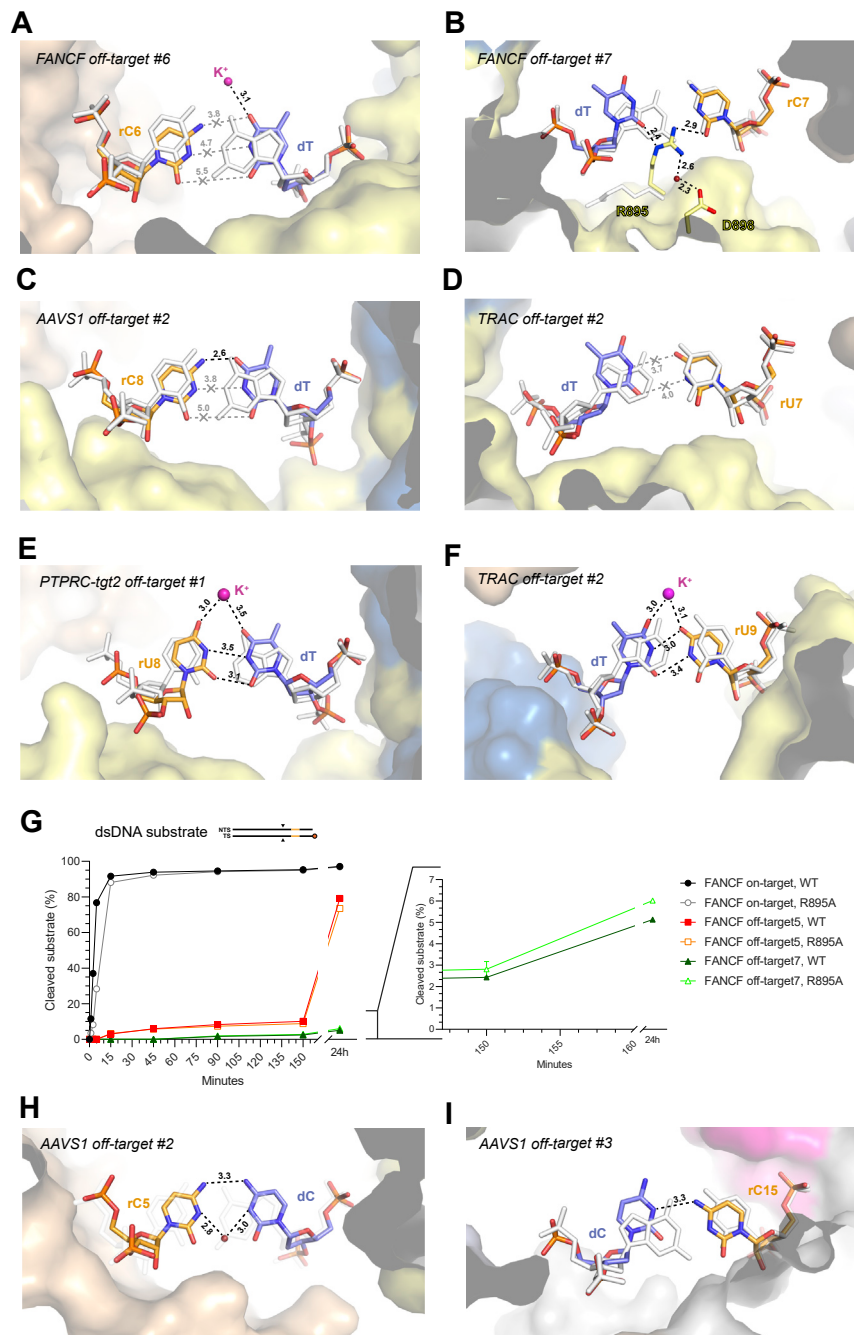


Figure S5. Pyrimidine-pyrimidine mismatches within off-target complexes, related to Figure 3

(A) Close-up view of rC-dT mismatch at position 6 in *FANCF* off-target #6 complex.
 (B) Close-up view of rC-dT mismatch at position 7 in *FANCF* off-target #7 complex, bridged by Cas9 Arg895 side chain. The Arg985 side chain in the corresponding on-target complex is shown superimposed and colored white.
 (C) Close-up view of rC-dT base pairing at position 8 of *AAVS1* off-target #2.
 (D) Close-up view of rU-dT mismatch at position 7 in *TRAC* off-target #2 complex.
 (E) Close-up view of rU-dT pairing at position 9 in *PTPRC-tgt2* off-target #1 complex.
 (F) Close-up view of rU-dT pairing at position 8 in *TRAC* off-target #2 complex.
 (G) Kinetic analysis of *FANCF* on- and off-target substrate DNA cleavage by wild-type and R895A Cas9 proteins.
 (H) Close-up view of partially paired rC-dC mismatch at position 5 in *AAVS1* off-target #2 complex, bridged by a water molecule.
 (I) Close-up view of rC-dC mismatch at position 15 in *AAVS1* off-target #3 complex. Corresponding on-target base pairs are shown superimposed and colored white. For *PTPRC-tgt2*, the *FANCF* on-target structure was used and bases were mutated *in silico*.

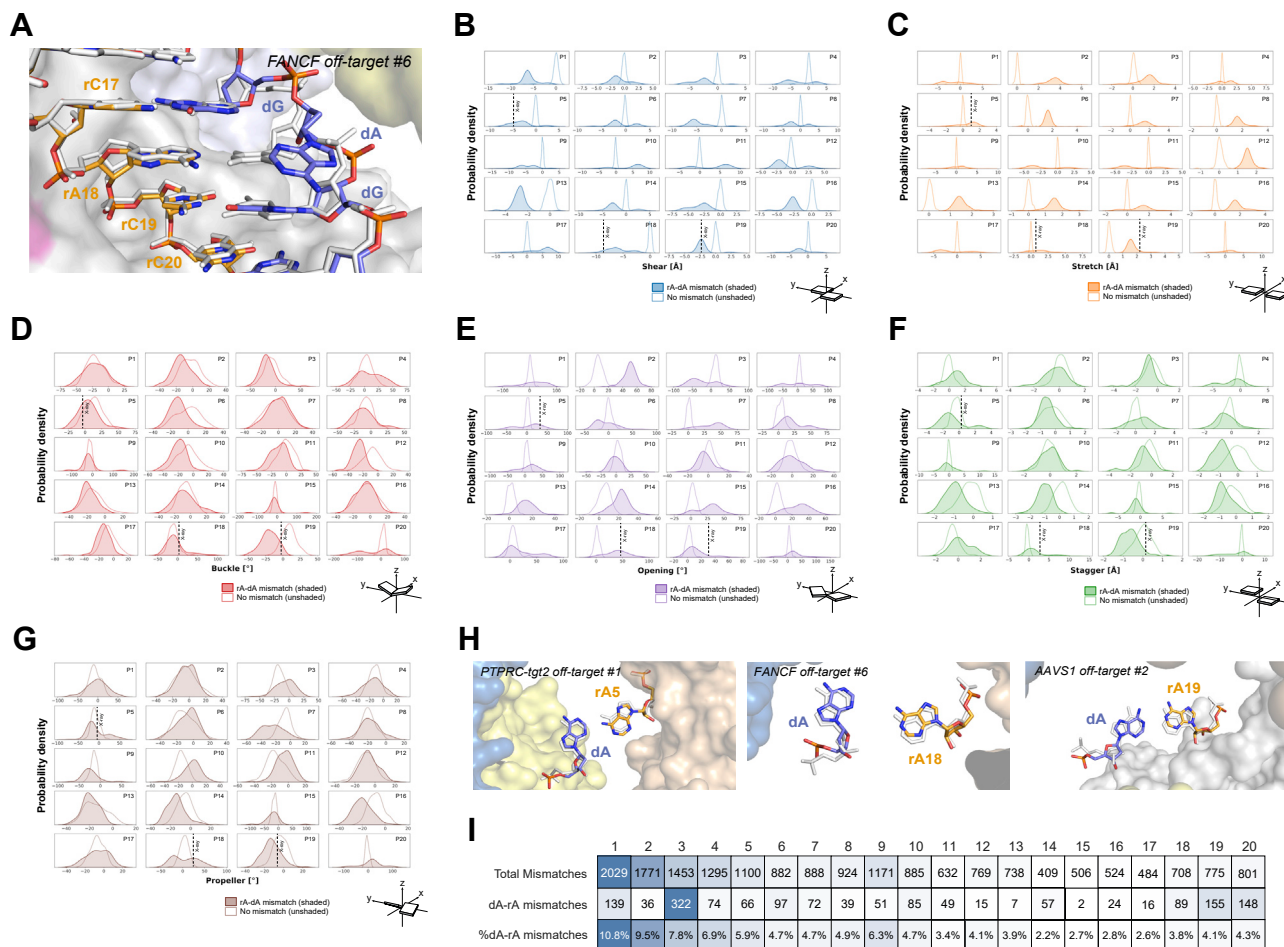


Figure S6. Position-specific conformation of off-target rA-dA mismatches, related to Figures 3 and 4

(A) Close-up view of rA-dA mismatch at heteroduplex position 18 in the *FANCF* off-target #6 complex, overlaid with the *FANCF* on-target structure (white). (B–G) Molecular dynamics analysis of rA-dA mismatches. Probability density plots for (B) shear, (C) stretch, (D) buckle, (E) opening, (F) stagger, and (G) propeller twist for the rA-dA mismatch at different heteroduplex positions, as computed from molecular dynamics simulations for the systems with (shaded) and without mismatches (unshaded). Vertical line in positions 5, 18, and 19 indicates base pair parameter value of the respective crystal structures. For each system, data are reported considering an aggregate sampling of $\sim 1.5 \mu\text{s}$.

(H) Close-up view of MD-simulated rA-dA mismatches (colored), overlaid with experimental crystal structure (white) at positions 5 (PTPRC-tgt2 off-target #1), 18 (*FANCF* off-target #6), and 19 (AAVS1 off-target #2).

(I) Number of rA-dA off-target mismatches per heteroduplex position recovered in the SITE-Seq assay for all analyzed genomic targets. Percentages indicate frequency of rA-dA mismatches recovered at the particular position as a fraction of total number of rA-dA mismatches.

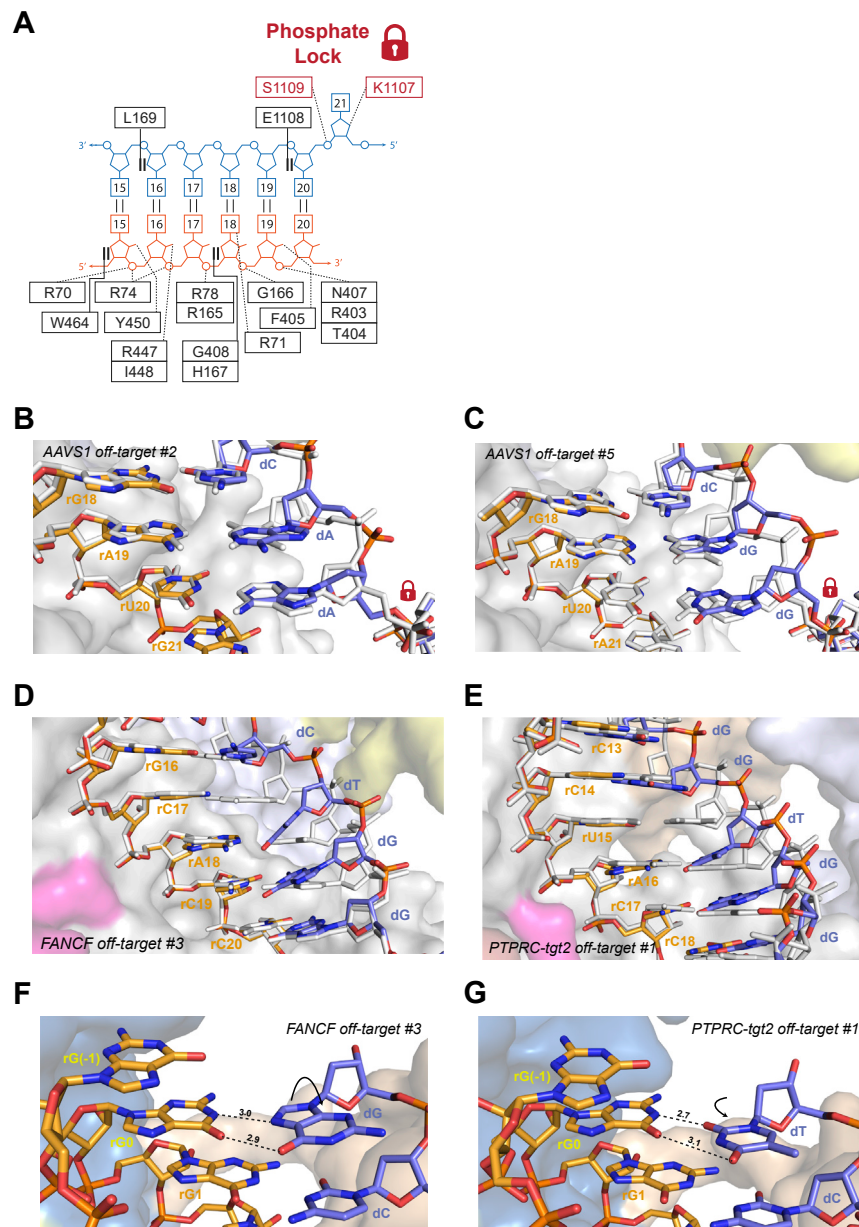


Figure S7. Lack of protein contacts with the target DNA strand in the seed region facilitates backbone distortions, related to Figures 4 and 5

(A) Schematic overview of Cas9 interactions within the PAM-proximal seed region of the guide RNA-TS DNA heteroduplex.

(B) Close-up view of the seed region in AAVS1 off-target #2 complex, overlaid with the AAVS1 on-target heteroduplex (white), showing structural distortion of the TS due to rA-dA mismatch at seed position 19.

(C) Close-up view of the seed region in AAVS1 off-target #5 complex, overlaid with the AAVS1 on-target heteroduplex (white), showing structural distortion due to rA-dG and rU-dG mismatches at positions 19 and 20, respectively. Red lock icon indicates position of the phosphate-lock residue in (B) and (C).

(D) Close-up view of base skip within the seed region of the guide RNA-off-target DNA heteroduplex in FANCF off-target #3 complex, overlaid with the on-target heteroduplex (white).

(E) Close-up view of base skip within the seed region of the guide RNA-off-target DNA heteroduplex in PTPRC-tgt2 off-target #1 complex, overlaid with FANCF on-target heteroduplex (white).

(F) Close-up view of noncanonical base pairs at the 5' end of the guide RNA in FANCF off-target #3 complex involving guanosine nucleotides introduced during *in vitro* transcription of the guide RNA.

(G) Close-up view of noncanonical base pairs at the 5' end of the guide RNA in PTPRC-tgt2 off-target #1 complex involving guanosine nucleotides introduced during *in vitro* transcription of the guide RNA.

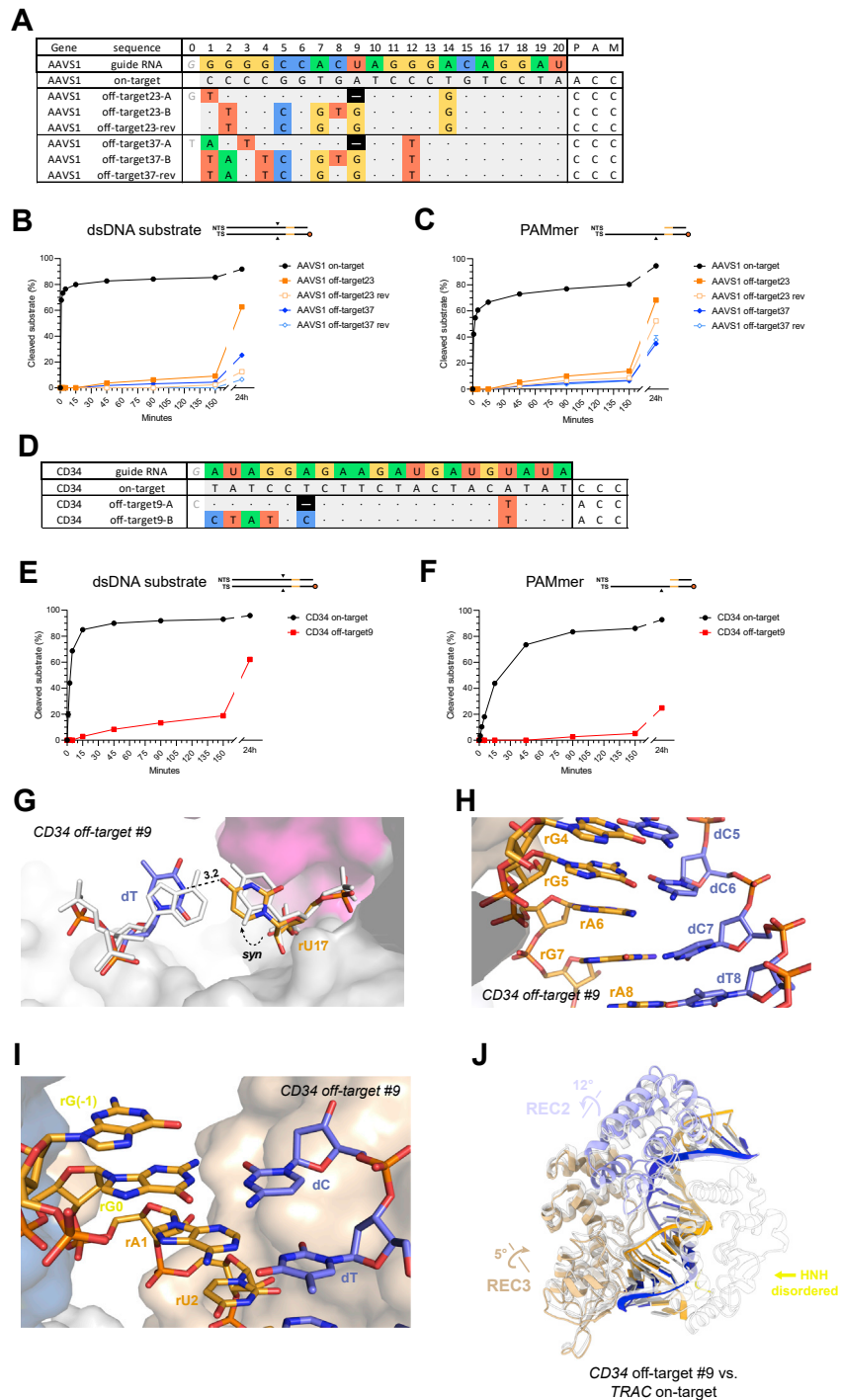


Figure S8. Accommodation of PAM-distal deletions by multiple mismatches or base skipping, related to Figure 5

(A) Schematic depiction of possible mismatch accommodation by multiple PAM-distal deletions (denoted “-A”) or formation of multiple mismatches (denoted “-B”) in AAVS1 off-targets. In off-target substrates denoted with “-rev”, a single nucleotide in the consecutive mismatch region is reversed to the corresponding on-target nucleotide.

(B) *In vitro* cleavage kinetics of fully double-stranded on- and off-target DNA substrates for off-targets with putative multiple consecutive mismatches in the PAM-distal region. Black triangles in the substrate schematic (top) indicate position of cleavage sites. Each data point represents a mean of four independent replicates. Error bars represent standard error of mean for each time point.

(C) *In vitro* cleavage kinetics of corresponding partially single-stranded (PAMmer) on- and off-target DNA substrates.

(D) Schematic depiction of a PAM-distal single-nucleotide deletion in the CD34 off-target #9 sequence.

(legend continued on next page)

(E) *In vitro* cleavage kinetics of fully double-stranded *CD34* on-target and off-target #9 substrates. Black triangles in the substrate schematic (top) indicate position of cleavage sites. Each data point represents a mean of four independent replicates. Error bars represent standard error of mean for each time point.

(F) *In vitro* cleavage kinetics of partially single-stranded (PAMmer) *CD34* on-target and off-target #9 substrates.

(G) Close-up view of rU-dT mismatch at position 17 in *CD34* off-target #9 complex. The corresponding on-target base pair (based on the *TRAC* on-target structure and mutated *in silico*) is overlaid and colored white.

(H) Zoomed-in view of the PAM-distal base skip at duplex position 6 in the *CD34* off-target #9 complex.

(I) Close-up view of rG-dC Watson-Crick base pair at the 5' end of the guide RNA in *CD34* off-target #9 complex, involving guanosine nucleotides introduced during *in vitro* transcription of the guide RNA.

(J) Structural overlay of the *CD34* off-target #9 complex with the *TRAC* on-target complex. The REC1, RuvC, and PAM-interaction domains have been omitted for clarity in all panels. The *CD34* off-target #9 complex domains are colored according to [Figure 1](#). The on-target complex is colored white.

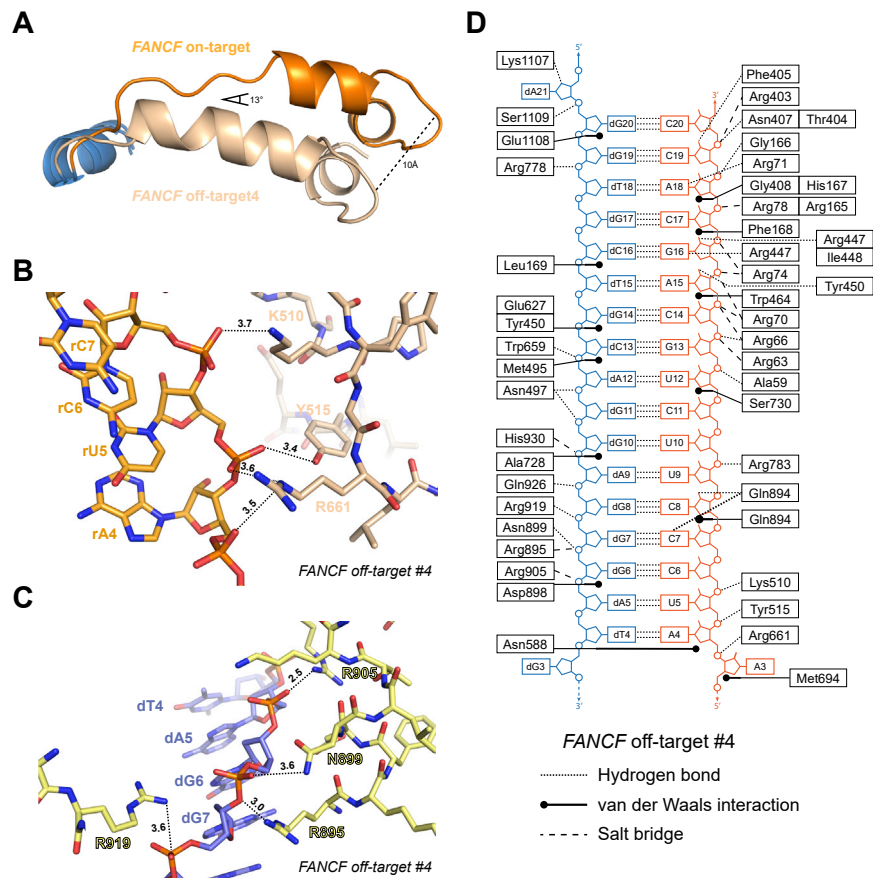


(figure continued on next page)

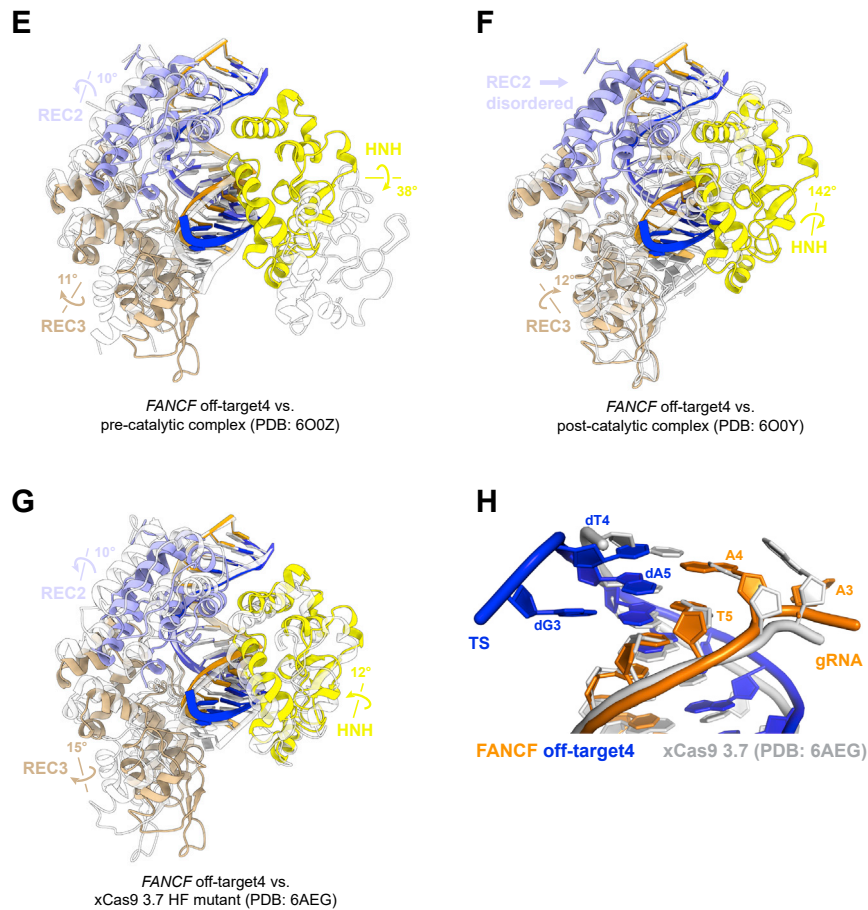


Figure S9. Altered heteroduplex interactions and conformational rearrangements in the *FANCF* off-target #4 complex, related to Figure 6

- (A) Overlay of REC3 domain helix (residues 703–712) in *FANCF* off-target #4 complex (wheat) with *FANCF* on-target complex (orange).
- (B) Close-up view of REC3 domain interactions with the guide RNA strand in *FANCF* off-target #4 complex.
- (C) Close-up view of TS DNA interactions established by HNH domain in *FANCF* off-target #4 complex.
- (D) Schematic depicting Cas9 residues interacting with the guide RNA:off-target DNA heteroduplex in *FANCF* off-target #4 complex. Dotted lines represent hydrogen-bonding interactions, dashed lines represent salt bridges, and solid lines represent stacking/hydrophobic interactions. Target strand is colored blue, guide RNA orange. Phosphates are represented by circles, ribose moieties by pentagons, and nucleobases by rectangles.
- (E) Structural overlay of the *FANCF* off-target #4 complex with cryo-EM structure of a pre-catalytic (state I) Cas9 complex (PDB: 6O0Z).
- (F) Structural overlay of the *FANCF* off-target #4 complex with the cryo-EM structure of a postcatalytic (state II) Cas9 complex (PDB: 6O0Y).
- (G) Structural overlay of the *FANCF* off-target #4 complex with the crystallographic structure of the high-fidelity xCas9 3.7 variant (PDB: 6AEG). The REC1, RuvC, and PAM-interaction domains have been omitted in all panels for clarity. The *FANCF* off-target #4 complex domains are colored according to Figure 1. The overlaid structures are colored white.
- (H) Overlay of the PAM-distal heteroduplex region in *FANCF* off-target #4 and xCas9 3.7 on-target complexes. Target strand is colored in blue; guide RNA is colored orange.